Department of Precision and Microsystems Engineering

Stability Limits for Capillary Aligned Micro-Parts Subject to High Dynamics

J.H.B. Horsthuis

Report no : 2022.032
Supervisor : Dr. ir. M. Tichem
Specialisation : Micro and Nano Engineering
Type of report : Master Thesis
Date : July 25, 2022

TU Delft Delft University of Technology

Challenge the future

Stability Limits for Capillary Aligned Micro-Parts Subject to High Dynamics

by

J.H.B. Horsthuis

To obtain the degree of

Master of Science
In Mechanical Engineering

At the
Department of Precision and Microsystems Engineering
Delft University of Technology

To be defended publicly on Tuesday July 25, 2022 at 12:30 PM.

Student number:	4375181	
Project duration:	September 1, 2021 – July 25, 2022	
Thesis committee:	Dr. ir. M. Tichem,	TU Delft, supervisor
	Dr. M. Mastrangeli,	TU Delft
	Dr. ir. R.A.J. van Ostayen,	TU Delft
	M.Sc. S. Soliman,	TU Delft

TU Delft

This MSc research project was made possible by the Delft University of Technology in collaboration with ITEC equipment and automation technologies B.V. Their corporation is hereby gratefully acknowledged.

Preface

I invite you to read this Master's Thesis project about the 'Stability Limits for Capillary Aligned Micro-Parts Subject to High Dynamics'. I have been working on this subject for a year, and I'm confident that I have learned a lot about this research field. This investigation was part of a bigger project conducted at the Delft University of Technology in collaboration with ITEC equipment and automation technologies B.V.. During the project, I appreciated being part of a bigger team. I enjoyed the regular meetings with people from different fields with whom I had some exciting discussions.

I could not have accomplished this study and thesis on my own. Therefore I would like to thank several people. First of all, my supervisor, Marcel Tichem, for all the great advice and guidance he has given. Furthermore, I would like to thank Thijs Blad for his support during my experiments and for helping with the setup. Also, I would like to thank Max Mastrangeli for sharing his knowledge and for all the fruitful discussions we had about this topic. These people and the rest of the team created a pleasant environment I enjoyed being a part of.

After all these years, my time as a student has finally ended. The subject of this Master's Thesis is an excellent summary of all the aspects I have learned in my Mechanical Engineering bachelor's and master's. Static and dynamic engineering, fluid mechanics, MATLAB programming, vibration analysis, etc. I hope you enjoy reading this thesis as much as I enjoyed working on it.

J.H.B. Horsthuis
Delft, July 2022

Abstract

Capillary self-alignment shows the potential to keep small components aligned using soft liquid contact when disturbed by external forces. Whilst this concept has been promising, mostly static situations have been investigated, making it unclear how a receptor-droplet-chip (RDC) configuration behaves dynamically and where its stability limits are.

The primary aim of this research was to determine the stability limits of such a configuration and explore its failure modes. Two non-linear analytical models simulate the situation and investigate the parameters exposed to the system. These models predict the relative lateral displacement of the chip and its tilt, which can predict when failure should occur. Results from Surface Evolver, a computational software, and experimental data from a laboratory setup validate these models. A shaker induced one DOF linear accelerations, and high-speed cameras observed these tests. The validated model was then used to investigate the effects of variables such as lubricant height, chip dimensions and acceleration magnitudes.

This project gives an insight into how a chip behaves dynamically on a liquid meniscus and was the first to investigate the tilt of the component during accelerations. The key finding is a stable region showing what amount of liquid results in reaching the highest possible acceleration without failure. Secondly, the models and experiments showed that smaller liquid volumes and chip sizes increase the attainable acceleration. Chips of $L = 2mm$ were able to be accelerated up to $a = 27g$ without failure, parts of $L = 1mm$ even reached an acceleration of $a = 35g$ at which the RDC configuration remained intact. Moreover, possible eigenfrequencies were observed, and the system could re-align at specific frequencies from a tilted pose. Therefore, this research has demonstrated that, under the right conditions, capillary interfaces can be useful to transport components under high accelerations.

Contents

List of Figures

List of Tables

Nomenclature

β	Tilt angle of the component
γ	Surface tension of water
μ	Dynamic viscosity of water
ϕ	Topological angle of a solid
ρ_s	Density silicon
ρ_w	Density water
θ	Edge angle of a liquid pinned at a solid
θ_0	Contact angle of an unpinned liquid at a solid
a	Constant acceleration
a_{peak}	Peak acceleration
A_m	Lateral surface area of the meniscus
Bo	Bond number
d_s	Peak-to-peak distance between displacements
d_v	Vertical displacement of a corner of the component
E	Surface energy
f	Frequency
F_a	Inertial force of the component
F_c	Capillary restoring force
F_v	Viscous force of the liquid
g	Gravitational constant
h	Total height of the lubricant from the receptor's surface to the chip's corner
h_0	Lubricant height
I	Inertia of the component
k	Lateral stiffness of the meniscus
L	Length of the component
L_{cap}	Capillary length
L_m	Centre of gravity for half the pad
m	Mass of the component and liquid combined
m_c	Mass of the component
p	Pressure
r	Radius cylinder
t	Time
T	Torque
th	Thickness of the chip
v	Lateral velocity of the liquid
V	Liquid volume
x	Lateral shift of the component relative to the receptor

1 Introduction

1.1. Motivation

As of today, one of the biggest global markets estimated at 483 billion dollars in 2022 and projected to grow to 893 billion dollars in 2029 is the semiconductor market [1]. According to the Semiconductor Industry Association, 1.15 trillion semiconductor units were shipped only in 2021 [2]. In perspective, just over 36,000 units every second must be produced to reach that goal. Since this number will keep increasing and the assembled parts will decrease in size, existing machines must be improved to keep up with the demand. Therefore, the Precision and Microsystems Engineering department of the Delft University of Technology has collaborated with ITEC Equipment and Automation Technologies B.V. (ITEC) to find innovations that can improve the assembly speed and quality of semiconductor parts. Some examples of these devices are LEDs (light-emitting diodes), photocells for solar panels and ultra-thin chips [23, 51]. Fig. 1.1 shows examples of these mounted parts.

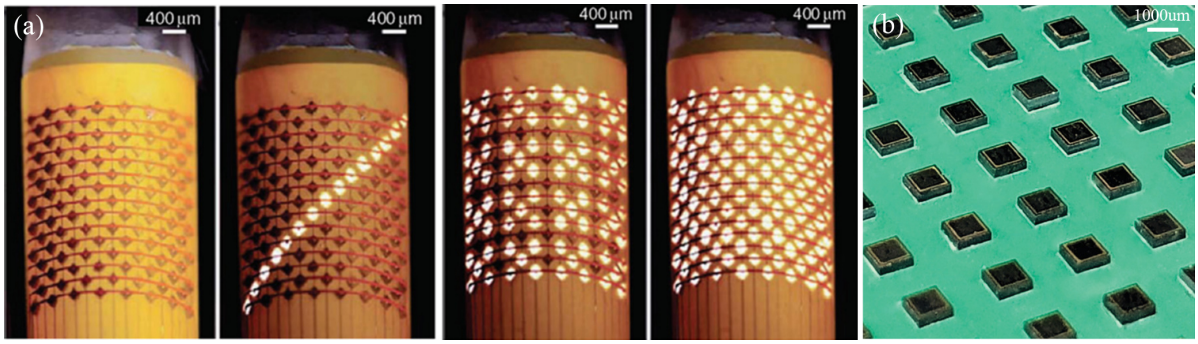

Figure 1.1: Two examples of microparts that have been assembled using fluidic self-assembly. (a) Micrographs of a cylindrical display with LEDs [21]. (b) Picture showing photocells for solar panels [43].

Nowadays, machine-based micro handling is the current industry standard in precision assembly, a well-performing method capable of assembling thousands of components per hour [44]. However, this pick-and-place method is limited by its assembly speed, especially when handling parts of sub-millimetric size. Contact handling may also damage the object, and the process is not easy to parallelize. In some cases, substrates have become flexible and non-planar, making it difficult for these methods to work with [5, 21].

1.2. Capillary Self-Assembly at High Dynamics

Overcoming drawbacks such as limited assembly speed and damage due to contact handling requires new principles and methods. Self-assembly may solve these problems since it is a parallel process, bonding multiple parts simultaneously, and capable of providing high throughput with sub-micron alignment accuracy [11, 28, 48]. More specifically, surface tension-driven or capillary self-alignment has proven to be a technique that is still capable of maintaining its liquid configuration when subjected to relatively high forces. The method is based on the stress generated on fluid surfaces; placing a chip on top of a droplet can increase

that. Surface energy in this fluid interface leads to capillary forces trying to minimize the energy and obtain a balance. These forces can align small chips to the desired position. Especially at more minor scales, these capillary forces become relatively large compared to the gravitational and inertial forces of the chip.

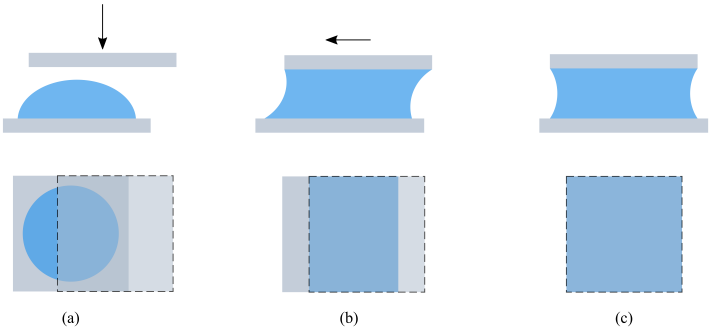

Figure 1.2: Side-view (top) and top-view (bottom) of the whole capillary alignment. Grey rectangular shapes on top and at the bottom are the microchip and receptor site. The blue shapes are the liquid. (a) Microchip being placed on a droplet. (b) Meniscus forms a liquid bridge between receptor pad and microchip. (c) Capillary forces move the chip towards the receptor's centre until the meniscus's final equilibrium shape is reached. Figures are based on multiple figures from several papers [13, 39].

The whole process of capillary self-assembly can be divided into three subsequent phases. First, chip release with a given direction, speed and accuracy, Fig. 1.2 (a). Often, vacuum tweezers, micro grippers or, for example, laser die transfer are used. Secondly, the chip touches the surface of a droplet of liquid, Fig. 1.2 (b). A receptor site usually confines this droplet. This is the position on a plate or substrate on which the chip must be assembled or kept in place. A wetting contrast - a hydrophilic receptor on a hydrophobic plate - is a possible method of confining a droplet, but also edges or a combination of both can be used [8, 46]. When the chip touches the droplet, a meniscus forms between the surface of the receptor and the chip, where capillary forces align it to the receptor site. After the chip has crossed the mean position of the receptor for the first time, its motion continues. After moving further, it moves back and forth, oscillating until it has reached its final position, Fig. 1.2 (c).

The advantages of capillary self-assembly over other techniques using contact handling are extensive. As the size of parts decreases, it becomes more difficult for these handling methods to maintain their precision and speed [5, 21]. Capillary forces and their alignment performance increase when the parts are downscaled. Moreover, some objects being handled are sensitive to contact handling and require a soft or non-contact handling method. Capillary assembly is capable of delivering this. At the same time, some alternatives deliver these solutions. Systems using micro-gel grippers, optical tweezers or even acoustic levitation exist that provide non-contact gripping of small parts [17, 19, 20]. However, capillary assembly does not use the positioning of actuators but solely uses the passive alignment capabilities of the fluid.

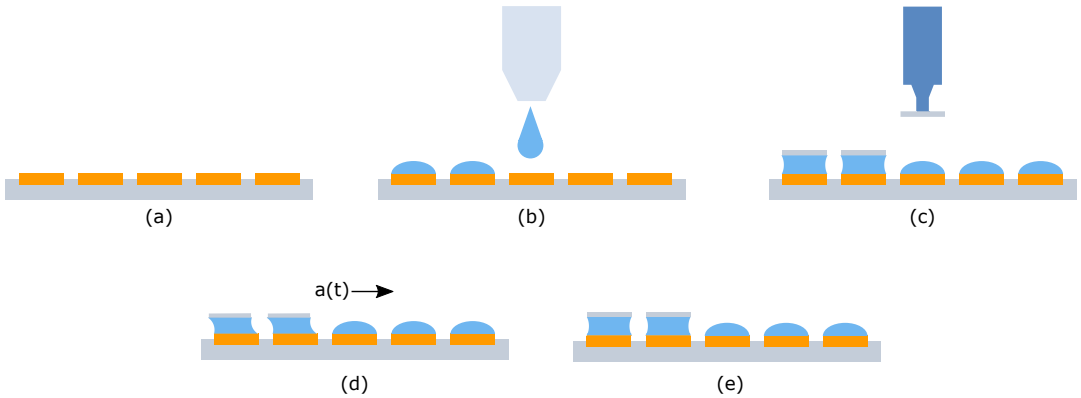

Figure 1.3: Overview showing how capillary self-assembly can be implemented in a system. (a) Empty substrate (grey) with receptor sites (orange). (b) Fluid deposition. (c) Component placement with vacuum tweezer (dark blue). (d) Lateral acceleration of substrate. (e) Rest position.

A schematic overview illustrating how a machine could implement capillary assembly is represented in Fig. 1.3. This figure shows a substrate with receptors at which components must be aligned. First, a droplet is deposited and confined at the receptor site, followed by the placement of a chip. Now, a configuration exists in which a liquid bridge connects the receptor with the component. In order to place another part on top of a different receptor site, the whole substrate must accelerate and decelerate to reposition underneath the vacuum tweezer. In 2025, ITEC aims to build a machine capable of assembling 1M parts per hour. Achieving this goal requires parts to accelerate up to 60g without failing. This research will mainly focus on the step shown in Fig. 1.3 (d), at which these accelerations occur.

1.3. State of the art

Previous to this MSc research project, a literature study was performed to find state of the art related to fluidic self-assembly. This chapter shows the most important outcomes of this investigation. The literature study itself shows the additional details and explanations of these outcomes. Moreover, state of the art relevant to the specific topic of this MSc research is shown at the end of this chapter.

1.3.1. Fluidic Self-assembly Fundamentals

Generally, two approaches can model a static system with an RDC. One is the energetic approach; the other method is Laplace's law. Most studies have used one of these two methods to make an analytical approximation of the problem. Usually, it gives a simple idea of what should happen in experiments. More powerful tools that give more precise solutions are software such as Surface Evolver or Comsol Multiphysics.

Often droplets are confined by a wetting contrast in which a hydrophilic receptor is placed on a hydrophobic substrate. Generally, a wetting contrast seems to provide a better alignment accuracy than when edges are used, but it is unclear where this difference originates. Examples do exist of studies that use an edge solely instead. A combination of a wetting contrast and edges is a hybrid confinement method of which only its wetting performance has been studied. Future work could focus on fluidic self-assembly using a hybrid method. This could result in better wetting capabilities and better assembly performance.

Author	**Year**	**Confinement**	**Part size**	**Accuracy**
Tsai *et al.*	2007	Edge	1 mm	16 μm
Sariola *et al.*	2010	Edge	50-300 μm	2-3 μm
Zhou *et al.*	2006	Edge	300 μm	5-10 μm
Srinivasan *et al.*	2001	Wetting contrast	150-400 μm	< 0.2 μm
Sato *et al.*	2003	Wetting contrast	0.8-1.0 mm	< 5 μm
Knuesel *et al.*	2010	Wetting contrast	20-60 μm	0.9 μm
Fukushima *et al.*	2011	Wetting contrast	3 mm	0.5 μm
Chang *et al.*	2017	Wetting contrast	500 μm	1.4 μm

Table 1.1: Overview showing differences in accuracy for part size and methods [9, 18, 23, 40, 41, 45, 46, 52].

The shape of the micro part is very much dependent on the final application it should fulfil. In most cases, the parts are rectangular, but recent studies also show circular shapes. The size of most studied chips lies in the range of 100 to 500 microns. Only a few studies show experiments done with chips smaller than 100 microns. Since there is a trend in downscaling electronic parts, more knowledge of assembling smaller parts is required.

In order to obtain a high yield and high alignment accuracy, it is recommended to match the shape of the component and receptor. However, it is possible to assemble chips and receptors with different shapes. A certain amount of jaggedness of the chip is also allowed to align the chip still. This concept might be relevant for industrial applications since it is allowed to have imperfections. The number of allowed defects on chips could increase the total yield.

1.3.2. Process Integration

Fluidic self-assembly consists of two integrated sub-processes: fluid deposition and chip placement. Fluids can be deposited with single droplet methods, which are relatively slow but offer more control over droplet volume size. Parallel methods such as spraying mist or dip-coating have higher throughput, but the placement and volume size of the droplets are more difficult to control. Fig. 1.4 shows four different fluid de-

Author	Year	Shape	Parts	Time	Yield
Srinivasan *et al.*	2001	Rectangular	98	1 min	100%
Xiong *et al.*	2003	Rectangular	16	2 min	88%
Fang *et al.*	2005	Rectangular	164	3 min	100%
Zheng *et al.*	2006	Rectangular	600	2 min	100%
Fang *et al.*	2006	Rectangular	1000	2 min	100%
Park* *et al.*	2010	Rectangular	116	1 min	90-100%
Knuesel *et al.*	2010	Rectangular	62500	45 sec	98-100%
Park* *et al.*	2012	Rectangular	81	70 sec	100%
Park* *et al.*	2013	Circular	90	1 min	100%
Park* *et al.*	2014	Rectangular	15000	60 min	>99%
Cho *et al.*	2019	Circular	19663	1 min	99.90%

Table 1.2: Overview showing differences in shape, assembled parts, the time it took to assemble and the final yield. *These studies are published by the same author showing the same experimental setup that is improved in every study [10, 15, 16, 33–35, 37, 45, 49, 51].

position methods [29]. Future research could focus on droplet jetting or inkjet printing to deposit fluids or parallelize other existing single droplet methods. The parallel processes lack knowledge in both modelling and experimenting.

There seems to be a trade-off in lubricant volume concerning the capillary forces and yield. A smaller lubricant volume increases the capillary forces, increasing the alignment speed and improving the final alignment. However, the yield increases for larger volumes. How this trade-off works and how this can be useful for making design choices could be investigated more thoroughly in future works. Moreover, studies investigating the effect of lubricant volume on the assembly performance used receptors with edges or a wetting contrast. It is unclear if these effects are the same when using hybrid methods. A recessed receptor, combined with a wetting contrast, could offer a more significant lubricant volume while keeping a relatively small gap between the receptor's and component's edges.

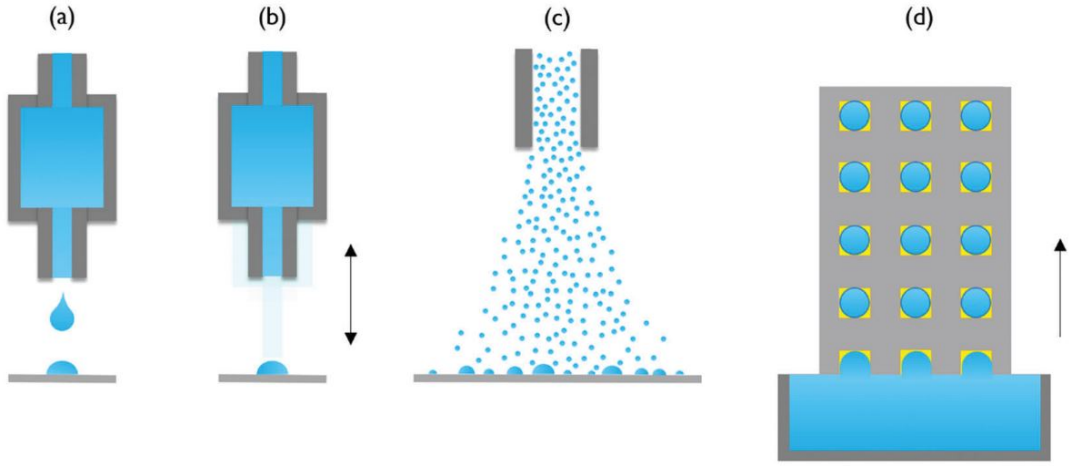

Figure 1.4: Most common methods of fluid deposition. (a) Non-contact single droplet (b) Contact single droplet (c) Parallel stochastic (d) Parallel deterministic [29].

Components can be fed to receptors one by one, parallel, using fluidic agitation and vibration feeding or floatation feeding. Single component methods are relatively slow and place the parts with a relatively low precision but offer a deterministic placement method. On the other hand, laser die transfer offers a single-component technique that theoretically reaches a very high throughput of 100 million parts per hour. Therefore, combining this with fluidic self-assembly seems an interesting topic that requires more research. Vibration and agitation methods often require many chips compared to the available receptors on the substrate. For example, one study used over three million chips to fill approximately 19,000 receptors. The efficiency of these methods could therefore increase in future research.

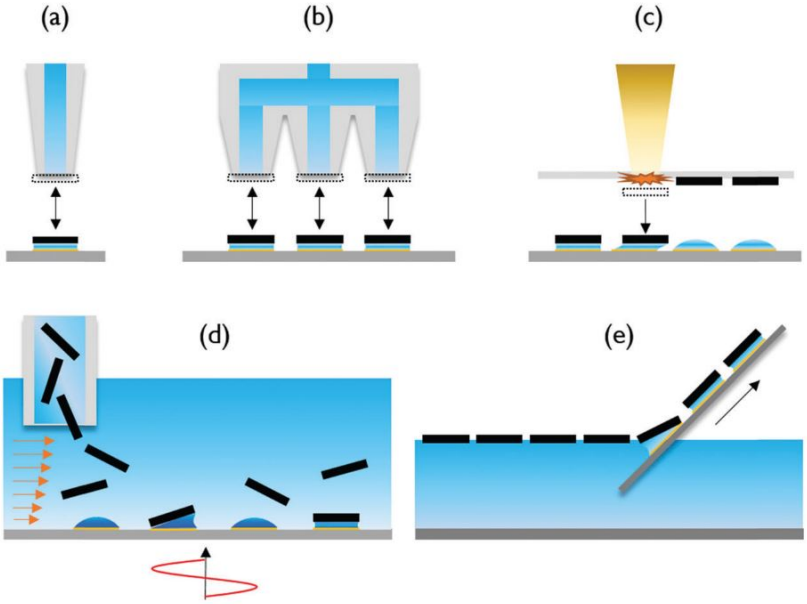

Figure 1.5: Component feeding techniques with a) single-component feeding, b) parallel multi-component pick-and-place, c) laser-induced-transfer d) fluidic agitation and vibration feeding e) floatation feeding [29].

Controlling the orientation of chips can be done by using magnetic fields and pulling magnetized parts of the chips in a specific direction. Another method is forcing the chip into an orientation by using shape recognition. Matching a low-order symmetric shape of both the chip and receptor could achieve this. The downside of both methods is that they require adaptations of the chips. Future research could focus on the orientation control of the chips without changing them.

1.3.3. Capillary Self-assembly Dynamics

Most models describing alignment dynamics use a combination of Navier-Stokes and Newton, coupling the lubricant's liquid flow with the component's inertial forces. Often these models are used for situations described in 2D, making the models less complex and easier to solve. Studies have modelled 3D situations, enabling them to study multiple deformation modes simultaneously. However, this drastically increases the computational time. If computing power increases soon enough, the research could focus more on building models in 3D.

Author	Year	Model details	Experiments	Validity
Zhang *et al.*	1990	1D-coupled, Navier-Stokes	None	-
Perales *et al.*	1991	2D-coupled, Young-Laplace	TV camera	Excellent
Meseguer *et al.*	1995	2D-coupled, Young-Laplace	Compared with existing literature	Good
Park *et al.*	2001	2D-coupled, Mean-field model	None	-
Martinez *et al.*	2004	2D-coupled, Duffing oscillator	CCD cameras	Poor
Meseguer *et al.*	2005	2D-coupled, Lyapunov-Schmidt	CCD cameras	Excellent

Table 1.3: Overview showing different studies describing a liquid bridge with models based on meniscus shape [27, 31, 32, 36, 38, 50].

Few studies have focussed on the dynamics after the alignment and how forces influence the system's stability. Parameters such as viscosity and lubricant volume influence the stability of a liquid bridge. However, these studies all consider a situation in which both the receptor and component are fixed. No studies are yet available investigating the stability of a meniscus in which the component can move freely along the liquid. Moreover, these studies lack knowledge of parts of sub-millimetre size. Only one study investigated the shift of a component after accelerating and decelerating the substrate. Future research could focus on modelling situations with a freely moving component and perform experiments to validate these models.

1.4. Problem Statement & Research Question

Fluidic self-assembly might be a suitable method to improve, for instance, the assembly speed of pick-and-place methods. Much knowledge is available about how to confine the droplets, what types of chips to use and other aspects of process integration. Furthermore, many studies investigated static modelling and even the dynamics of the chip alignment process. However, implementing fluidic self-assembly into a machine also requires knowledge about the dynamic behaviour after the chip alignment. After the alignment of a chip, it is, for example, desired to know what the acceleration limits are to improve the throughput of that machine. Models exist of such cases describing the stability of a liquid bridge between two solids, but only in situations where these are fixed. The highest acceleration speeds that have been experimented with are approximately $30g$, whilst most machines in the industry accelerate well above those speeds. A method is required in which the dynamical behaviour of an assembled chip can be modelled and observed using experiments.

The above-mentioned leads to the following problem description:

'Current assembly methods do not deliver both the desired throughput and placement precision of chips any more. Fluidic self-assembly might be a solution to that, but models describing the dynamical behaviour of an aligned chip do not exist yet or are in most cases not suitable enough. Besides, almost no experiments have been conducted to investigate the design limits of an aligned configuration.'

This Master's Thesis project aims to develop a method in which analytical models and experiments demonstrate the stability limits of a microchip aligned with fluidic self-assembly subjected to acceleration forces. Parameters such as the height of the lubricant, chip size and acceleration magnitude are varied to investigate their effect on the stability of the liquid bridge under acceleration. The research question relevant to this study is as follows:

'What are the limits to the alignment capabilities of a liquid bridge between receptor and component subject to high accelerations?'

To support this research question, a set of three fundamental sub-questions are given as well:

- What failure modes exist that disrupt the liquid bridge and what causes these to happen?
- How can the lateral displacement and tilting of the component during accelerations be modelled?
- What methods exist to predict when a component is lost during transport due to accelerations?

2

Stability Limits of the System

In order to answer the research question, it is essential to understand the dynamics of a receptor-droplet-chip (RDC) configuration and to find the restricting stability boundaries of such a system. The visualization in Fig. 2.1 shows an isometric view of such a configuration. A liquid connects a chip to a receptor on the bottom. This receptor is a thin rectangular square with equal dimensions to the chip. It can contain a droplet because the liquid will pin along all its edges. The line along these edges is an interface at which a gas from the surroundings, a liquid from the meniscus and a solid from the receptor or chip come together. This line is referred to as the triple line, or contact line [24]. Capillary forces act along these lines to keep the system balanced. Implementing capillary alignment in high dynamics systems introduces external forces, deforming the droplet and moving the top chip. If these deformations and displacements become too large, the meniscus might break or even eject the chip completely. Since these accelerations are relatively high, the configuration is expected to function close to its instability region.

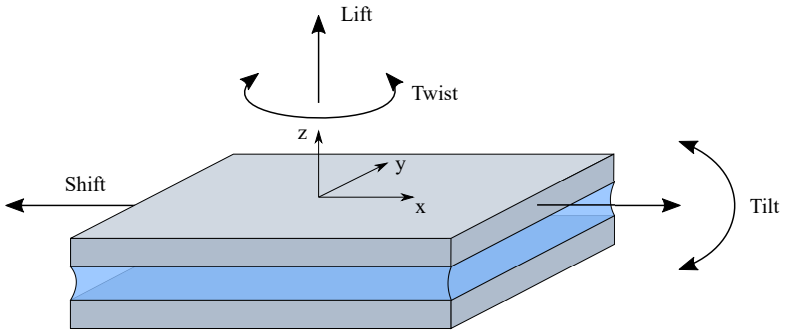

Figure 2.1: Illustration of an RDC configuration in which the displacement modes have been indicated with arrows.

Four displacement modes of a square chip have been recognized [4]. A shift is a lateral displacement relative to the receptor along the x- or y-axis. Roll or tilt are rotations about the x- or y-axis. In the case of a square chip, these are equivalent. Lift and twist represent the vertical displacement along and a rotation about the z-axis. This study has focussed on both shift and tilt and how these may cause unpinning of the meniscus or result in dry friction between receptor and chip. This chapter focuses on two models predicting the shift and tilt of a component during accelerations. The possible failures due to these deformation modes are shown, giving the stability boundaries of the system.

The main objectives of this chapter are:

- Understand the parameters and variables that play a role in dynamics of the system and how large their influence is.
- Approach the configuration with a simple yet effective model.
- Find the most important aspects causing failure of the system due to accelerations.

2.1. Failure Modes

Ideally, an evenly distributed liquid bridge connects the receptor and chip and is pinned on all edges. Due to accelerations of the receptor, the meniscus starts deforming, resulting in displacements of the top chip. These deformations may cause unpinning of the contact lines, dry friction or even rupturing of the liquid. This section describes these failure modes in more detail.

2.1.1. De-wetting and Contact Angle Hysteresis

As mentioned before, accelerations of the receptor will result in a lateral shift and tilt of the top chip. It is essential to understand in what situations the contact lines stay pinned and when they start to unpin. This will help predict when de-wetting will occur. This principle is related to the angle the liquid makes with a solid. For example, the angle θ shown in Fig. 2.2 is the edge angle between the liquid surface and the solid along the entire edge. This contact line will stay pinned for specific values of this angle, and for some values, it will start to unpin. This is related to the ability to confine droplet inside a receptor and can be expressed by the Gibbs' inequality condition [46]:

$$\theta_0 \leq \theta \leq (180^o - \phi) + \theta_0 \tag{2.1}$$

Here, θ is the edge angle of the liquid on the solid edge, θ_0 is the contact angle, and ϕ is the geometrical angle of the solid. The contact angle θ_0 is the angle the water surface makes with a smooth solid surface when it is not pinned, as seen in Fig. 2.2 on the right. For example, if the angle $\phi = 90^o$ and $\theta_0 = 25^o$, the contact line will stay pinned if its value remains between

$$25^o \leq \theta \leq (180^o - 90^o) + 25^o = 115^o \tag{2.2}$$

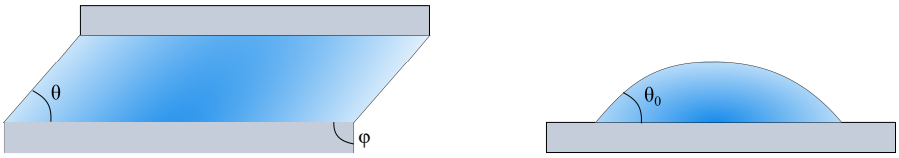

Figure 2.2: Two figures showing an RDC configuration on the left and an unpinned droplet on a smooth surface on the right. Here, θ corresponds to the edge angle, ϕ to the topological angle of the solid and θ_0 to the contact angle.

When one of these values exceeds the boundaries, the contact line at the edge will start to unpin. This causes the meniscus to slide across the surface or to flow over the edge. In the first scenario, the unpinned edges might be able to move back again and pin to the edges. After overflowing, most configurations will fail because the system cannot restore itself.

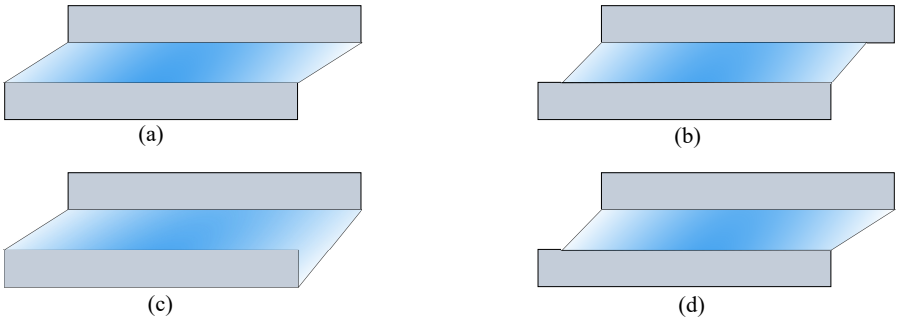

Figure 2.3: Overview of four possible scenarios during motion. (a) Pinned (b) Two edges unpinned (c) Overflow (d) One edge unpinned. Figures based on [30].

In the above situations, only a lateral shift is considered, and the top chip's tilting motion or vertical displacement has been neglected. In those situations, the edge angles in the opposite corners are the same. In reality, tilting motions of the chip also occur, resulting in four different edge angles. In Fig. 2.4 the difference between only a shift and a situation with both shift and tilt can be seen. In the first situation, $\theta_1 = \theta_3$

and $\theta_2 = \theta_4$. While in the right situation $\theta_1 > \theta_3 > \theta_4 > \theta_2$. This shows that the angles will become different when tilting is included, meaning that the boundaries described in Gibbs' inequality criterion might be exceeded more quickly. Therefore it is also important to consider the tilting motion of the chip to create a more conservative model.

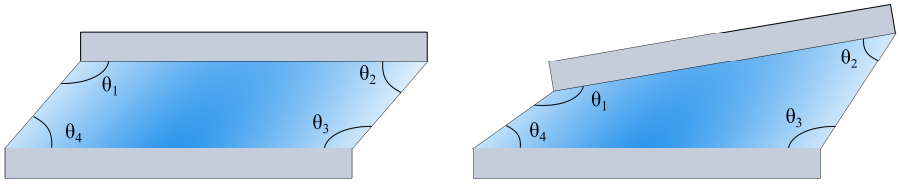

Figure 2.4: Figures showing the difference in edge angles for a situation in which only lateral shift is considered (left) and a situation with both lateral shift and tilting motion of the chip (right).

At the beginning of this chapter, Fig. 2.1 shows a situation in which the meniscus surface is not straight but rather concave. Figures are often illustrated this way because the meniscus shape is concave at the corners between the receptor and chip. However, in environmental conditions with water in air, the shape is straight along the edges between the surfaces. An example of what this looks like can be seen in Fig. 2.5. This shape has been confirmed by experiments and simulations performed in Surface Evolver. Screenshots of these can be found in Fig. 3.2 and Appendix A. Another reason why figures are often shown with concave surfaces is that for large displacements and a constant water volume, the meniscus' shape becomes slightly hyperboloid [31]. Since these concave shapes are only located at the corners and are challenging to implement into a model, they are not considered.

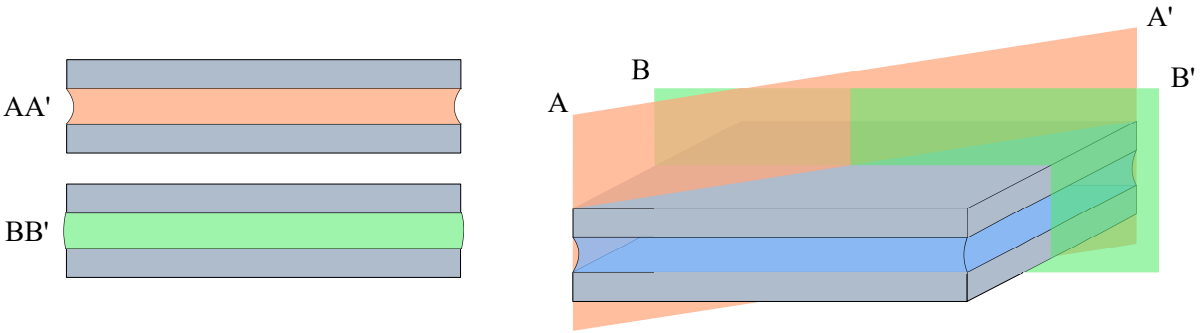

Figure 2.5: Sketches showing the difference in cross-section from different cut-planes of the configuration on the right. The colour of the liquid refers to the cross-section taken on the right. Figure based on [7].

2.1.2. Dry Friction and Rupture

Another failure mode that might occur due to the tilt is dry friction. Due to the tilting motion of the chip, the edges on the left and right are moving up and down towards the receptor site. If this displacement is large enough, they might come in contact. These friction forces may be significantly large to keep the chip from moving and preventing a smooth alignment with the receptor. Therefore, it seems necessary to find a model capable of predicting how much tilt will occur in what situations.

When accelerations are high enough, a component could be ejected completely [7]. Usually, this happens only with relatively large chip sizes (>5mm). This is because the inertial force of the chip's increased mass become more significant. Moreover, this is very complex to predict and is therefore not considered in this study's models.

2.2. Numerical 1D State Space Model

At first, a linear state-space model was made to predict how large the lateral shift would be under different circumstances. The model is based on the system shown in Fig. 2.1 on which several assumptions have been made to simplify the problem. The receptor site accelerates, and only the lateral shift and edge angles are calculated. In this model, the surface tension is translated into lateral stiffness and the viscous force into lateral damping. By doing this, the system is approached as a mass-spring-damper placed on top of a massless cart. The found trends from this model related to some of the variables are similar to that of the model described in the next section. However, the actual results related to the shift and edge angles turned out to be less accurate than the non-linear model. This is because, in the situations described here, the displacements are relatively large and thus non-linear. Therefore, this model is not described in more detail but can still be found in Appendix B.

2.3. Numerical 1D Non-linear Model: Shift

This section presents a non-linear model in which the bottom receptor accelerates, resulting in a lateral shift of the top chip relative to the receptor. The model gives an insight into how some variables affect this shift. Moreover, the shift can be used to predict what the edge angles will be. At the end of this section, insights and trends are presented and discussed. This model was based on an existing model and adapted to a new situation [7]. Here, both the receptor and chip are considered square rigid objects with side lengths L and thickness th. The meniscus is a deformable parallelogram with a non-changing height of h_0 and neglecting tilt. This height is assumed to be smaller than the capillary length $L_{cap} = \sqrt{\gamma/\rho_w a(t)} < \sqrt{\gamma/\rho_w g}$ (i.e. $Bo << 1$). Usually, only the gravitational effects are considered. However, the accelerations in this situation (up to $60g$) are significantly higher than the gravitational constant ($g = 9.81 m/s^2$), leading to a capillary length of $L_{cap} \approx 350 \mu m$. Moreover, the surfaces are assumed to be ideally smooth and chemically homogeneous. This should lead to smooth unpinning of the triple contact line upon de-wetting.

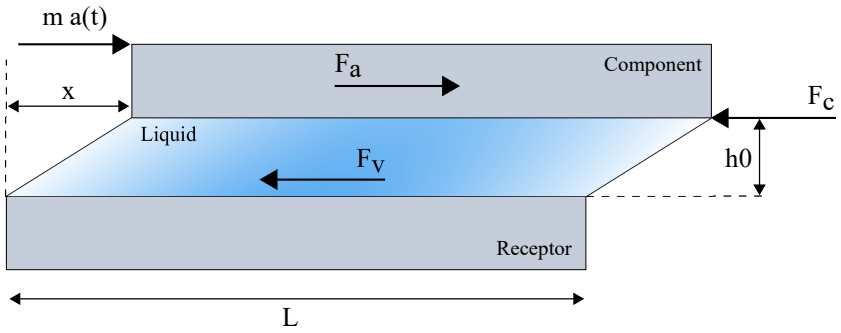

Figure 2.6: Two-dimensional representation of the system showing a liquid bridge connecting a component to a receptor. F_v and F_c represent the viscous and capillary force, whereas F_a represents the inertial force of the chip.

2.3.1. Liquid and Solid Physics

When the receptor is in motion, Newton's equation for rigid bodies can be used [7]. In this situation, the acceleration of the receptor generates an inertial force F_a, but also a viscous force F_v exists due to a velocity profile in the liquid and a restoring capillary force F_c because of the relative displacement and deformed droplet. The acceleration induced by the receptor is introduced to the system and described as $F_i = -ma(t)$. This system's visualisation with the relevant forces can be seen in Fig. 2.6. This results in

$$m_c \frac{\delta^2 x_c}{\delta t^2} - F_v - F_c = -ma(t) \tag{2.3}$$

in which m_c and x are the mass and position of the chip, and $a(t)$ is a non-constant acceleration which is multiplied with a mass m equal to the weight of both component and liquid. The first coupling term in this model is the viscous force F_v, given as

$$F_v = \mu L^2 \frac{\delta v_x}{\delta z}\Big|_{z=h0} \tag{2.4}$$

where μ is the dynamic viscosity and v_x the lateral velocity of the liquid [13]. The velocity is found by solving the Navier-Stokes equation for an incompressible fluid of density ρ_w between two plates separated by a distance h_0.

$$\frac{\delta v_x}{\delta t} - \frac{\mu}{\rho_w}\frac{\delta^2 v_x}{\delta z^2} = -a(t) \tag{2.5}$$

Initially, the system is at rest, and a no-slip condition at the surfaces of the receptor and component is assumed. The initial boundary conditions are given as follows:

$$\begin{cases} v_x(z,t=0) &= 0 \\ \frac{\partial v_x}{\partial t}(z,t=0) &= 0 \\ x(t=0) &= 0 \\ \dot{x}_c(t=0) &= 0 \\ \ddot{x}_c(t=0) &= 0 \end{cases} \quad \text{and} \quad \begin{cases} v_x(z=h_0,t) &= \dot{x}_c \\ v_x(z=0,t) &= 0 \end{cases}. \tag{2.6}$$

The second coupling term is the restoring capillary force F_c. It acts at the contact line and tangent to the gas-fluid interface and is proportional to the length of the edge L and the surface tension γ. This restoring force can is derived from the minimization of the surface energy of a liquid [25]. If the shift of the component is small enough, it does not change the height of the gap, but it does increase the lateral surface area of the meniscus, which is found by

$$A_m = 2Lh_0 + 2Lh_0\sqrt{x^2 + h_0^2} \tag{2.7}$$

Here, the gap height and length of the sides of the chip are denoted as h_0 and L. The lateral displacement is represented by x. The surface energy E in this situation is given as

$$E = \gamma A_m + C \tag{2.8}$$

where C is an arbitrary constant. Now, the restoring force can be found by deriving the equation with respect to d:

$$F_c = -\frac{\delta E}{\delta x} = -\frac{2\gamma L x}{\sqrt{x^2 + h_0^2}} \tag{2.9}$$

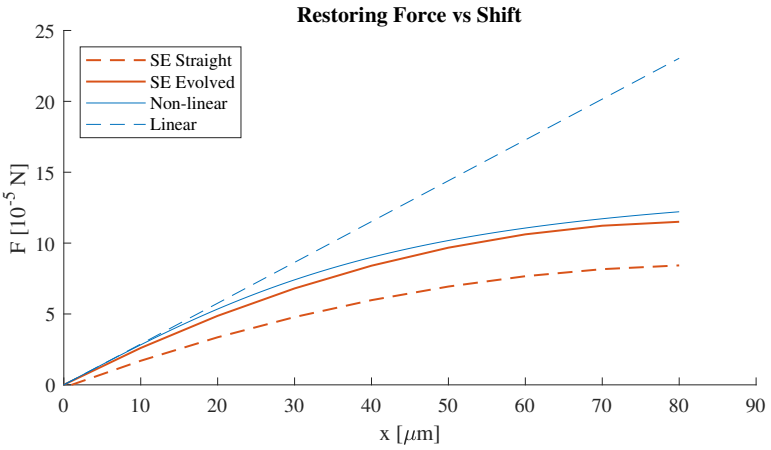

Figure 2.7: Plot of the linear and non-linear restoring force. Compared with results of Surface Evolver. Here, a $L = 1mm$ chip has been used with lubricant height $h_0 = 50\mu m$. The system is assumed to be in environmental conditions.

The restoring force can be calculated for increased displacements. The plot in Fig. 2.7 shows the differences between the non-linear restoring force used here, a linearised force used in the linear model, and a comparison made with Surface Evolver (SE). Additional explanations of the differences between a straight and evolved surface made with SE can be found in Appendix A. Note that the direction of the force is opposite to the displacement. This non-linear approximation is valid for a larger range of deformations and will therefore be used in this model [30]. The lateral stiffness is found by taking the derivative of the restoring force concerning the displacement x:

$$k = \frac{\delta F_c}{\delta x} = \frac{2\gamma L h_0^2}{(x^2 + h_0^2)^{3/2}} \tag{2.10}$$

This model is solved by using a non-constant acceleration $a(t)$ as input and solving it numerically with the Runge-Kutta method at each time step in MATLAB.

2.3.2. Results and Discussion

This section shows and discusses the results and trends recognized from the model. The investigated variables of interest are the acceleration magnitude a, lubricant height h_0 and chip dimensions. The simulations were performed by giving the model a sinusoidal acceleration $a(t)$ as input and calculating the maximum lateral shift x as an output. The following parameters have been used to obtain the results:

Symbol	Name	Value	Unit
ρ_s	Density silicon	2300	kg/m^3
ρ_w	Density water	1000	kg/m^3
μ	Dynamic viscosity	$8.9 \cdot 10^{-4}$	$Pa \cdot s$
γ	Surface tension	0.0728	Nm^{-1}

Table 2.1: Parameters that have been used in the model to obtain the results in this subsection.

First, the variation in acceleration magnitude and lubricant height are presented. Fig. 2.8 displays two graphs in which, on the left, the lateral shift of the chip is shown versus an increasing acceleration magnitude. Several lubricant heights have been fixed to demonstrate how the displacement increases for higher accelerations and how this changes for different lubricant heights. A similar graph is given on the right, in which the lubricant height is increased. Here, some acceleration magnitudes have been fixed, showing the effect on shift.

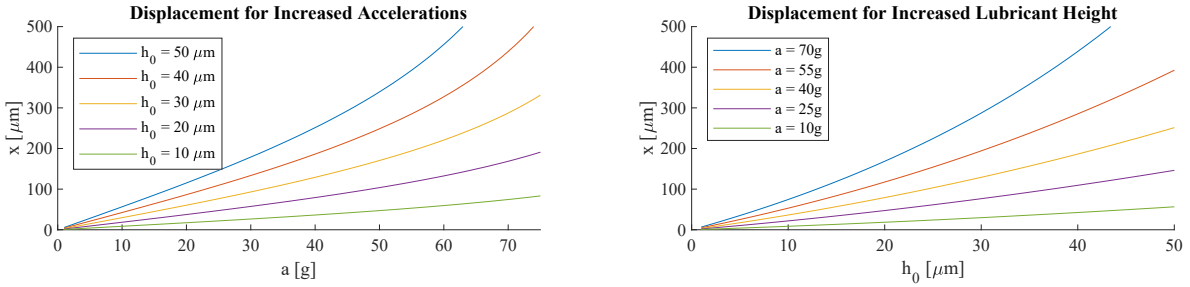

Figure 2.8: Graphs showing the effects of an increase in acceleration (left) and an increase in lubricant height (right) on the lateral displacement of the top chip relative to the receptor. Here, chips of $L = 1mm$ and $th = 50\mu m$ are used.

Both graphs reveal similar characteristics. As expected, larger accelerations and lubricant height increase the lateral shift. The results show linear patterns for smaller values of both a and h_0. Whereas for acceleration values higher than $40g$ the results become slightly parabolic and, therefore, non-linear. On the other hand, the lubricant height seems to show a more linear trend than the increased acceleration magnitudes. The model was expected to behave linearly for smaller displacements, as explained in formula 2.9. Moreover, a contour plot is used to show the effect of both the acceleration magnitude and the lubricant height on the lateral displacement demonstrated in Fig. 2.12. This graph shows that an increase in lubricant height increases the shift relatively more quickly than an increase in acceleration. Therefore, it would be relevant for

industrial applications to decrease the lubricant height as much as possible to operate at the highest possible accelerations.

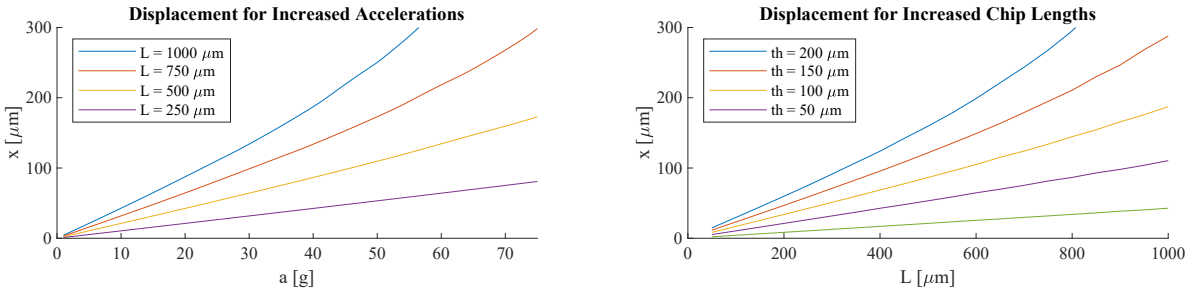

Figure 2.9: Graphs showing the effects of a change in chip dimensions. The side length L has been varied as well as the thickness th.

The other variables investigated are the chip dimensions L and th. The first graph in Fig. 2.9 shows the influence of the chip length for fixed constant thicknesses and increasing accelerations. The second graph demonstrates the effect of an increase in length L for different thicknesses. The graphs show a similar pattern as depicted in Fig. 2.8.

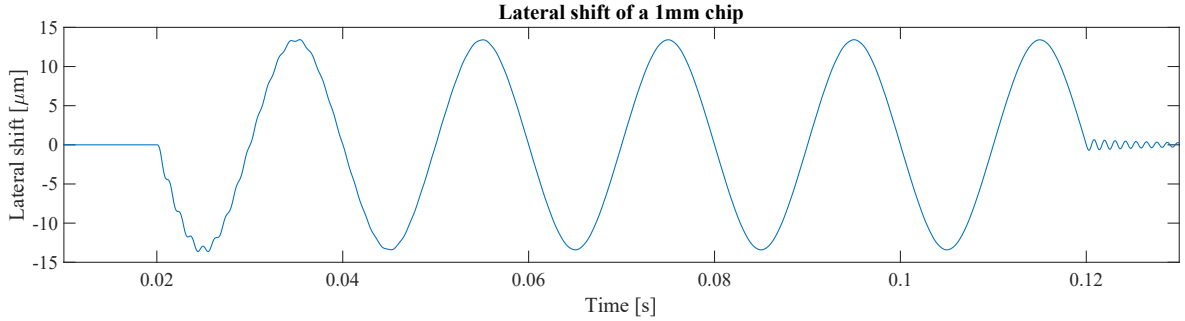

Figure 2.10: Graph showing the lateral shift relative to the receptor. Here, a $1mm$ chip was used and accelerated at $f = 50Hz$ with a magnitude of $a = 30g$. The lubricant height here was $h_0 = 40\mu m$.

The model can also approximate under what conditions failure due to unpinning of the contact lines will occur. This is possible since it predicts the lateral shift of the top chip for every time step. For example, if the receptor accelerates with $a = 30g$ at a frequency of $f = 50Hz$, the shift for every time step is displayed in Fig. 2.10. If, for instance, the contact angle of water with the solids equals $\theta_0 = 30^o$, the conditions under which the contact line stays pinned are $30^o \leq \theta \leq 120^o$, assuming that all solid edges have an angle of $\phi = 90^o$. The motion of the top chip can also be visualized. A screenshot of the chip at its maximum displacement is shown as well as the boundary conditions for the edge angles in Fig. 2.11.

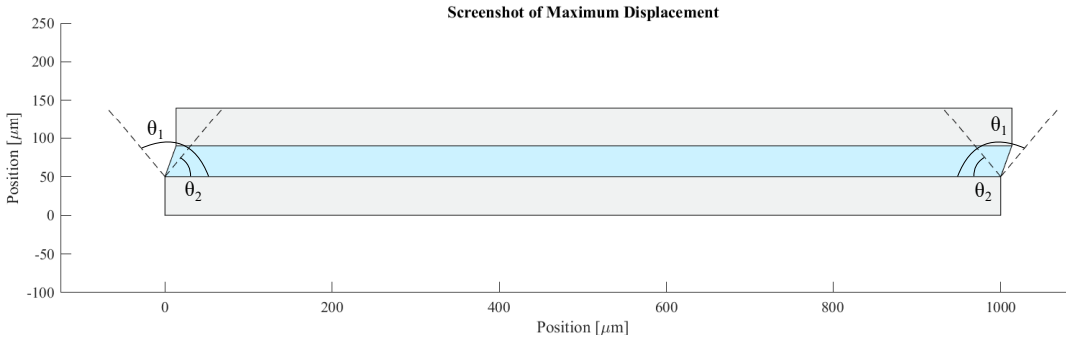

Figure 2.11: Screenshot of the visualization of the chip's lateral displacement. Here, the receptor and chip are shown in grey and the meniscus in blue. The angles $\theta_1 = 120^o$ and $\theta_2 = 30^o$ represent the boundaries of the edge angles. When these values are overridden, unpinning of the contact line will occur. Note, that the angles might seem bigger, but this can be explained by looking at the scales of both the x- and y-axis.

If the boundaries for the edge angles are $30^o \leq \theta \leq 120^o$, the maximum displacement for every combination of an acceleration magnitude and lubricant height can be calculated. For higher values of h_0, the displacement should be larger to reach the maximum allowed edge angle. However, increasing h_0 also decreases the lateral stiffness of the meniscus, which increases the shift. Results of the maximum shift of the top chip for different combinations of h_0 and a are visualized in a contour plot in Fig. 2.12. This plot can also be used to visualize constraints. The screenshot shown in Fig. 2.11 shows that in this exact position, the edge angle on the right is constrained by θ_1 and on the left by θ_2. The difference between θ_1 and θ_2 is always 90^o. An equally maximum displacement in both lateral directions can be reached if the contact angle is $\theta_0 = 45^o$. Now, the boundaries are $45^o \leq \theta \leq 135^o$. If the contact angle is increased or decreased, the boundaries will also change, and the maximum possible angle will be exceeded more quickly in one of the directions. In the contour plot, the dashed line represents combinations of h_0 and a at which an edge angle of exactly $\theta = 45^o$ is reached. The green region shows combinations resulting in angles smaller than 45^o, and in the red region, the combinations result in larger values and, therefore, unpinning and failure of the RDC.

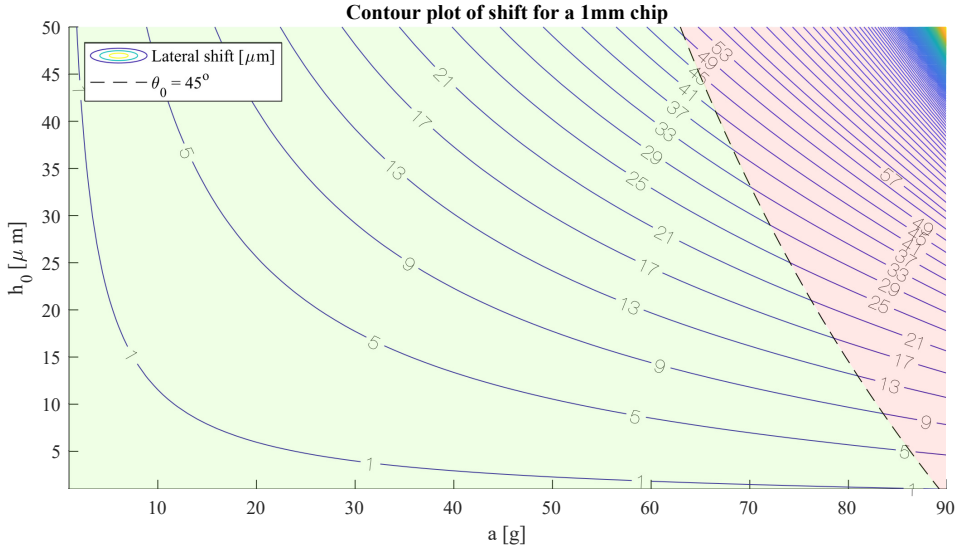

Figure 2.12: Contour plot showing the displacement for different combinations of lubricant heights and acceleration magnitudes. The dashed line indicates what combinations of h_0 and a result in an edge angle of exactly $\theta = 45^o$ or $\theta = 135^o$. If one of these values is exceeded, the system will unpin and cause the RDC to disrupt. The combinations at which this happens is indicated with a red. For combinations located in the green region, the system does not unpin.

The result of this graph suggests that the maximum acceleration that can be achieved without unpinning is $a = 90g$. Theoretically, for smaller values of the lubricant height, the displacement should always decrease and minimise the chance of unpinning. In theory, the constraint line should never cross the x-axis. However, in reality, there must be a maximum acceleration since the displacements cannot become infinitesimally small. Note that this plot is based on results for a $1mm$ sized chip. The possible acceleration magnitude without unpinning will change for smaller or larger chip sizes. Three examples of the limits for a $L = 2mm$, $L = 500\mu m$ and $L = 100\mu m$ can be found in Appendix C. In these cases, the acceleration limits were $a \approx 45g$, $a \approx 180g$ and $a \approx 900g$. This result also suggests that the system will still function within its stable region for considerable lubricant heights. However, there is a limit to this height that is not included here. There are studies indicating that there exists a critical volume for the droplet of RDC systems. This will be discussed in more detail in Section 2.5. Also, the constraint given in this contour plot is based on a contact angle of $\theta_0 = 45^o$. Changing this value will change the position of the constraint line as well. The effect of different contact angles is illustrated in Fig. C.4.

2.4. Numerical 1D Non-linear Model: Tilt

As mentioned in the previous model, dry friction might occur when the contact lines unpin, and the lubricant layer between the receptor and component disappears. Another reason that may cause this is the tilting motion of the chip. Moreover, tilt may also affect the edge angles and therefore unpinning at the edges may occur sooner than predicted in the previous model. Therefore, finding a model capable of predicting how much the chip will tilt during accelerations seems necessary. Here an existing model is used and adapted to predict the tilt for different magnitudes of shift [22].

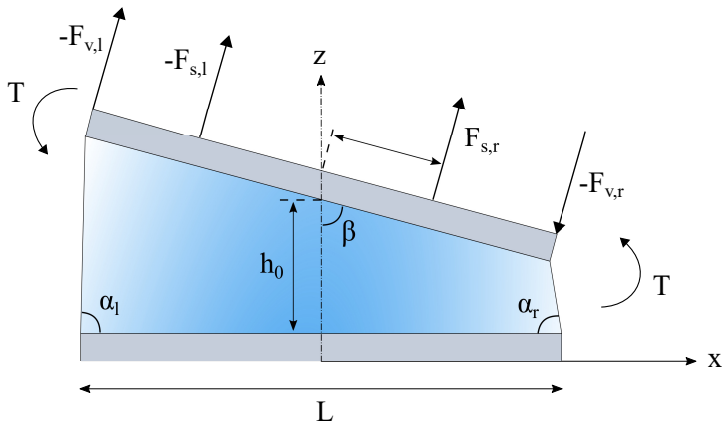

Figure 2.13: Chip on a droplet in a tilted position. Based on figure from [14].

Again, a square component with side lengths L and thickness th is connected with a liquid bridge to a receptor site with similar dimensions as the top chip. The meniscus is approached as a parallelogram. Only this time, the height at both edges is allowed to change. The height h_0, from the receptor to the centre of the chip's surface, does not change. Also, all heights are always smaller than the capillary length, and the surfaces are assumed to be smooth and chemically homogeneous.

2.4.1. Liquid and Solid Physics

During the tilting motion of the chip, the surface tension and viscous forces will be rotating. Since the surface tension forces are projected along the liquid surface, forces on the left-hand side of the chip are projected along a different angle than forces on the right. This means that a torque is applied onto the chip with equal inertial forces due to the rotating mass:

$$I\frac{\delta^2\beta}{\delta t^2} = T \tag{2.11}$$

Of which the angular momentum of the chip can be derived as

$$T = L_m(F_{\mathrm{s,r}} - F_{\mathrm{s,l}}) - \frac{L}{2}(F_{\mathrm{v,r}} - F_{\mathrm{v,l}}) \tag{2.12}$$

where L_m is the centre of gravity for half the pad, F_{s} and F_{v} are the surface tension and viscous forces. The subscripts l and r indicate whether the force is on the left or right-hand side. Figure 2.13 illustrates the situation with all the relevant dimensions and forces.

The viscous force is approximated as displayed in Fig. 2.14. Two vertical cylinders are assumed to support the component, and they alternatively expand and compress. Based on squeeze flow theory, a viscous force can be described mathematically that is required to realise these motions [14, 26]. The compressive force is given as

$$F_{\mathrm{v}}|_{\mathrm{compress}} = 2\pi\int_0^{r'} p(L,h)\,r\,dr \tag{2.13}$$

$$= \frac{3\pi\mu v L'^4}{2h^3}\left\{1 + \frac{4}{3}\left(\frac{h}{L'}\right)^2\right\} \tag{2.14}$$

in which p represents the pressure on the surface of one of the disks and r the radius of the disk. Now, the expansion force equals

$$F_{\mathrm{v}}|_{\mathrm{expand}} = -F_{\mathrm{v}}|_{\mathrm{compress}} \tag{2.15}$$

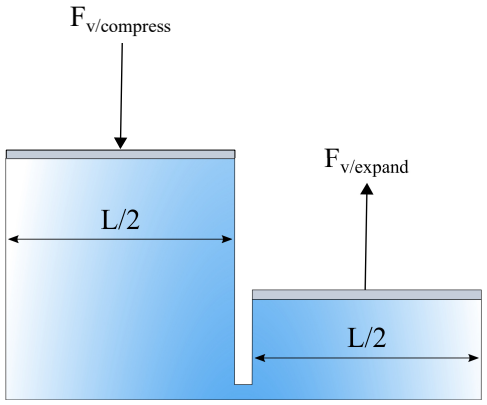

Figure 2.14: Schematic representation of the compressive and expanding viscous force during the tilting motion. Figure based on [14].

2.4.2. Coupling with Lateral Shift

Coupling the tilting motion of the chip with the lateral shift requires several simplifications to solve the model. First, both edge angles, α_l and α_r, at the bottom will be considered equal. This allows us to use the calculated surface tension forces of the first model from Section 2.3 for every time step. These values are used as input for the current model. This force must be transformed such that it projects in the same direction as the surface tension force in the current model:

$$F_{\mathrm{s,l}} = -F_{\mathrm{s,r}} = \frac{F_c}{2}\frac{h}{x} = -\frac{\gamma L h}{\sqrt{x^2+h^2}} \tag{2.16}$$

The capillary forces are calculated in the model from Section 2.2 and used as an input in the tilting model equation 2.12. The angle β and viscous forces depend on the free variable h, which leaves a second-order differential equation numerically solved by the Runge-Kutta method at each time step in MATLAB.

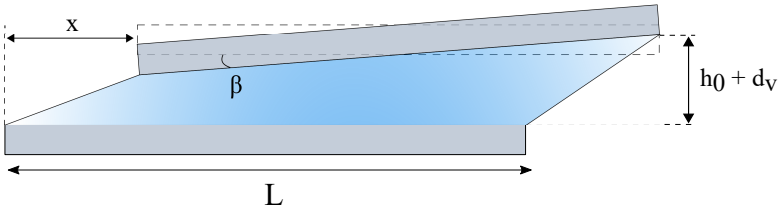

Figure 2.15: Figure illustrating how the results from the model described in Section 2.2 are used to find the tilting motion. The dashed lines indicate what the position is according to the tilting model. At this position, the centre height is kept the same and a tilt is introduced resulting in a vertical shift at the corners of the chip d_v. The total height is represented as $h = h_0 + d_v$.

2.4.3. Results and Discussion

The calculated outcomes of this model are the vertical shift of the top chip's left and right bottom corners. Moreover, the tilting angle of the chip β is calculated in degrees. Again, the variables that have been investigated are acceleration magnitude $a[g]$, lubricant height $h_0[\mu m]$ and chip dimensions. The following parameters have been used:

Since the vertical displacement and tilt are strongly dependent on the results from the model from Section 2.2, the variables a, h_0 and dimensions L and th show equal characteristics. The graph in Fig. C.6 shows that a change in h_0 affects the displacement more than a. The vertical displacement increases as well for an

Symbol	Name	Value	Unit
L	Length chip/receptor edges	1000	μm
th	Thickness chip/receptor	50	μm
ρ_s	Density silicon	2300	kg/m^3
ρ_w	Density water	1000	kg/m^3
μ	Dynamic viscosity	$8.9 \cdot 10^{-4}$	$Pa \cdot s$
γ	Surface tension	0.0728	Nm^{-1}

Table 2.2: Parameters that have been used to obtain the results in this subsection.

increase in both of these values. For acceleration values of $a > 50g$ and $h_0 > 40\mu m$ the results become slightly non-linear. Chips with smaller side lengths and thickness results in smaller displacements and lower tilting angles.

As in the previous model, the vertical shift relative to its starting position and the tilting angle for every time step has been visualized in C.5. The screenshot of the corresponding position at its maximum tilt and displacement is shown in Fig. 2.16. The four edge angles do not show symmetry, as with only a lateral shift. Now, every edge angle has a different value, with $\theta_a = 114^o$, $\theta_b = 74^o$, $\theta_c = 67^o$ and $\theta_d = 105^o$. Compared to the previous situation, the angles were $\theta_a = \theta_d = 108^o$ and $\theta_c = \theta_b = 72^o$. This shows a maximum difference of approximately 8^o, which is significant. The result of implementing this into a contour plot is shown in Fig. 2.17. This plot shows that when tilt is included, the accelerations at which unpinning occurs for equivalent gap heights have decreased to a value of $a \approx 75g$. This demonstrates that it is important to include the tilting motion of the chip as well to predict the unpinning.

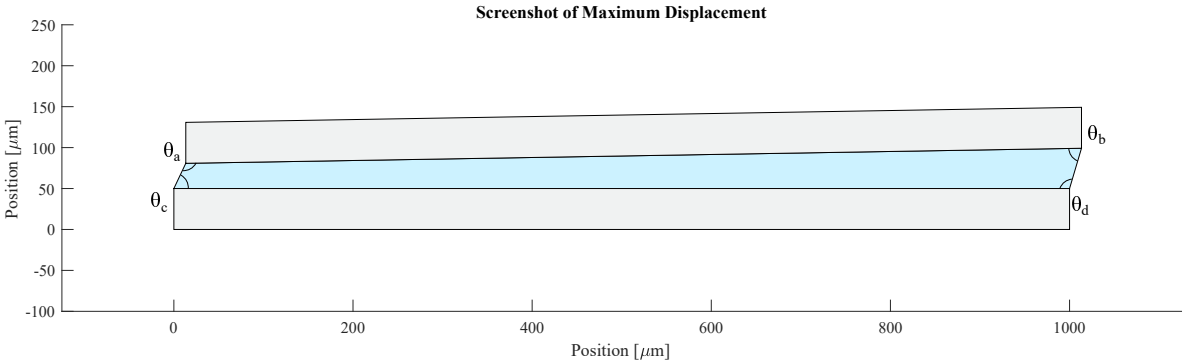

Figure 2.16: Screenshot of the maximum displacement and tilt after a $a = 30g$ acceleration with a lubricant thickness of $h_0 = 30\mu m$. In this situation the angles are $\theta_a = 114^o$, $\theta_b = 74^o$, $\theta_c = 67^o$ and $\theta_d = 105^o$.

It may happen that, when the tilting motions are large enough, the top chip will touch the bottom receptor at some point. The contour plot in Fig. C.6 shows how the vertical displacement of one of the corners of the top chip is dependent on different combinations of lubricant height and acceleration magnitudes. A significant result from this plot shows that the vertical shift will never be larger than the lubricant height. Thus theoretically, the top chip will never touch the bottom receptor.

2.5. Minimum and Maximum Critical Volume

The previous models described the lateral shift and tilt of the chip, but they did not mention any constraints concerning the minimum or maximum volume of the liquid. The concept of capillary length $L_{cap} = \sqrt{\gamma/\rho_w g}$ can be a useful tool to estimate the maximum gap height. Here, γ and ρ_w represent water's surface tension and density, and g is the gravitational constant. This constant is replaced with an acceleration a so that the capillary length can indicate the maximum height at high accelerations. For instance, a droplet of water in the air at room temperature has a capillary length of approximately $L_{cap} = 2.7mm$. If the gap h_0 is smaller than this length, the surface tension forces will dominate the external accelerations. According to the graph depicted in Fig. 2.18, the capillary length at $a = 80g$ is approximately $L_{cap} = 100\mu m$.

In most cases, the RDC will have a gap much smaller than the capillary length for all accelerations. Therefore, this concept is insufficient to constrain the maximum height h_0. Below the capillary length, too large

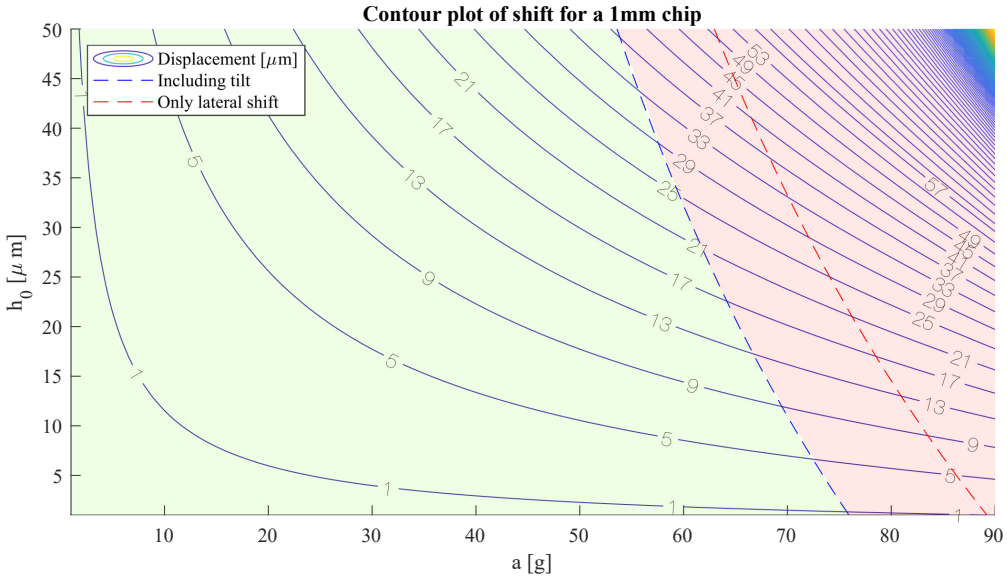

Figure 2.17: Contour plot showing the lateral displacement of a $1mm$ chip for different combinations of lubricant height and acceleration magnitude. Two constraint lines are implemented as well, representing the boundary of $\theta_0 = 45^o$. The red line shows the old situation in which only lateral shift is considered. The blue line includes the tilting motion as well. Again, the red region represents combinations of h_0 and a resulting in exceeding the boundary values of the edge angles causing the RDC to unpin. Combinations in the green region result in maintaining an intact RDC.

volumes of water can cause misalignment, and a tilted position of the chip [4, 42]. Contrarily, too little liquid might not be enough to wet both surfaces of the receptor and chip, resulting in dry friction between these two solids. Therefore, there might be an optimal value for the liquid volume to maximise the alignment capabilities and capillary forces. However, there is a lack of knowledge on how much liquid should be provided. For example, one study suggests that a gap height of $h_0 = 125\mu m$ should be used to obtain the best alignment performance of $1mm$ sized dies [3]. Another study mentioned that the highest yield of $300\mu m$ chips was achieved for volumes between $V = 1.8nL$ and $V = 2.7nL$, corresponding to heights of $h_0 = 19\mu m$ and $h_0 = 30\mu m$ [40]. However, these studies concerned static situations. Another recent study shows that the minimum required volume to capture a $600\mu m$ chip is $V = 2.5nL$, corresponding to a height of $h_0 = 7\mu m$ [7]. This indicates that the minimum required volume during accelerations can be, preferably, lower than during the capture of a chip. Since the minimum and maximum values cannot be calculated, these must be found experimentally.

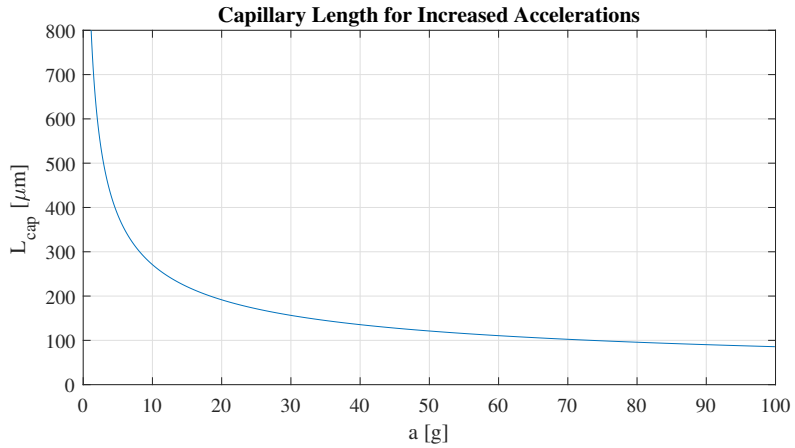

Figure 2.18: Capillary length in environmental conditions for an increase in acceleration.

3

Investigating the Stability Region

The previous chapter demonstrated several models that describe the dynamics of an RDC system subject to accelerations. A laboratory setup was built to get a better understanding of the reliability of these models and to gain new insights. Again, a system consisting of a receptor connected with a liquid bridge to a component is considered and subjected to high accelerations. Several experiments demonstrate the effects of some variables. Choices for these tests are explained first, followed by explanations of how these were performed and with what setup and materials.

The main objectives of this chapter are:

- Find suitable experiments to demonstrate the effects of parameters and variables of the system.
- Understand the most important variables and how large their influence is.
- Observe what failure modes occur, how often these take place and how these happen.
- Compare the found results with the previous shown models.

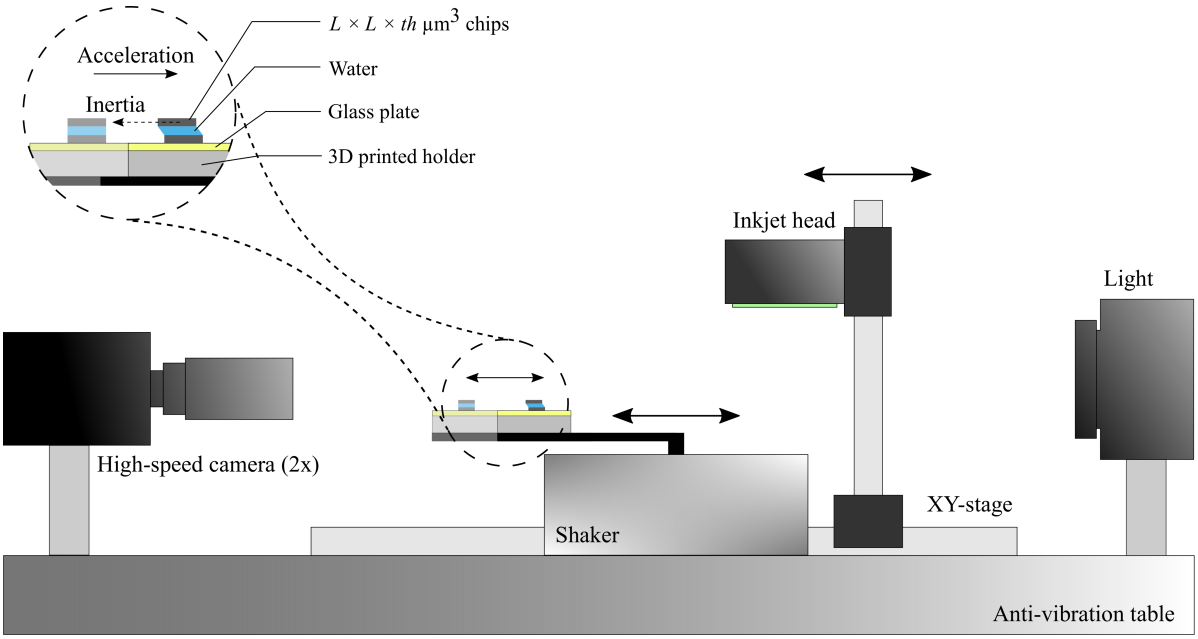

Figure 3.1: A square silicon chip is glued onto a glass substrate to function as a receptor. An inkjet head is used to deposit water on top of this droplet, whereafter a chip is deposited with tweezers. The glass substrate is connected to a shaker with a 3D printed holder. All observations are made with two high-speed cameras. One is placed directly in front of the substrate, a second camera is filming from an isometric perspective (not illustrated). Entire setup is placed on top of an anti-vibration table. Figure is based on a schematic from [7].

3.1. Experimental Setup

The setup used for the experiments is illustrated in Fig. 3.1. A square silicon chip of $L \times L \times th$ was glued on top of a glass substrate to function as a receptor. A minimal amount of epoxy kept the chip in place to preventing glue from spreading from under the component. A 3D-printed holder made from PLA keeps the glass substrate in place. This holder's design is such that the substrate is easily replaceable. The holder is mounted onto a shaker (TIRA Vibration Test System TV 51110) capable of delivering frequencies up to $7000Hz$ and accelerations up to $45g$. The components and liquid were handled with tweezers during the first experiments. In some cases, the liquid was deposited using an inkjet nozzle from an industrial printer, whose position is controlled by an XY-stage (Thorlabs - Linear Translation Stage). Two high-speed cameras (IDT-NX4 S1) did all observations, of which one camera was placed directly in front of the system (lens: Telecentric 58432), and the other filmed from an isometric perspective (lens: Telecentric 88346). A bright white LED shined towards the first camera, creating a high-contrast image. Typical pictures from the captured videos are shown in Fig. 3.2. All setup parts were placed on an anti-vibration table to prevent external forces and vibrations from disturbing the experiments.

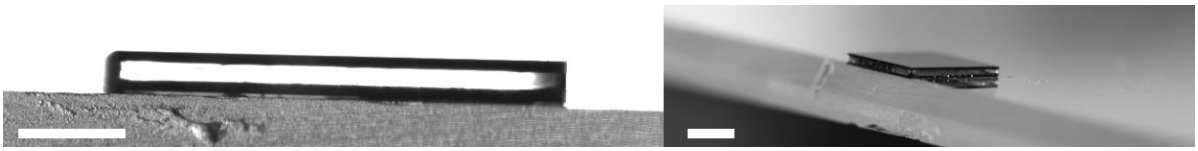

Figure 3.2: Pictures of an RDC system placed on top of a glass substrate. In both cases $2mm$ square silicon chips have been used as receptor and component. The picture on the left shows a front view of the system, scale bar = $250\mu m$. The picture on the right shows the same system from an isometric perspective, scale bar = $500\mu m$.

3.1.1. Generating Lateral Accelerations

The linear shaker is connected to an oscilloscope (Tektronix - TDS2014) and controlled with MATLAB. The input signals are sinusoidal, with a maximum number of periods and logarithmic frequency sweeps. Here, the signal's frequency $[Hz]$ and amplitude $[V]$ can be selected. The peak acceleration of these motions is found with an accelerometer but can also be calculated with

$$a_{peak} = \frac{(2\pi f)^2}{g} \frac{d_s}{2} \tag{3.1}$$

where f and d_s are respectively the frequency and peak-to-peak distance of the displacement, and g the gravitational constant ($= 9.81 m/s^2$). During initial tests, a discovery was made suggesting that the position of the shaker was drifting towards its mean position. The result is presented in Fig. 3.3, in which the position of the shaker was measured. Here, the input of the shaker is a total of 30 periods at a frequency of 200Hz with an output amplitude of approximately $70\mu m$.

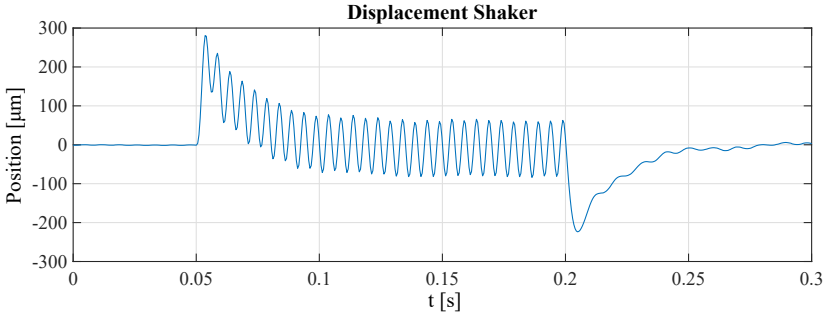

Figure 3.3: Graph showing the displacement of the shaker. A sinusoidal input was used with a frequency of $f = 200Hz$ and an amplitude of approximately $70\mu m$. The shaker started from rest after which it oscillated for a total of 30 periods up until it stopped.

This graph shows that the shaker takes about $t = 0.05$ seconds or ten periods to settle around its mean position. Other amplitudes show an equivalent pattern with approximately the same number of periods required to settle. Since the position is shifting, the length of every stroke cannot be the same, meaning

that the acceleration will be different at these peaks. Therefore, it is essential to perform experiments with a number of periods higher than the required ones to settle (>10).

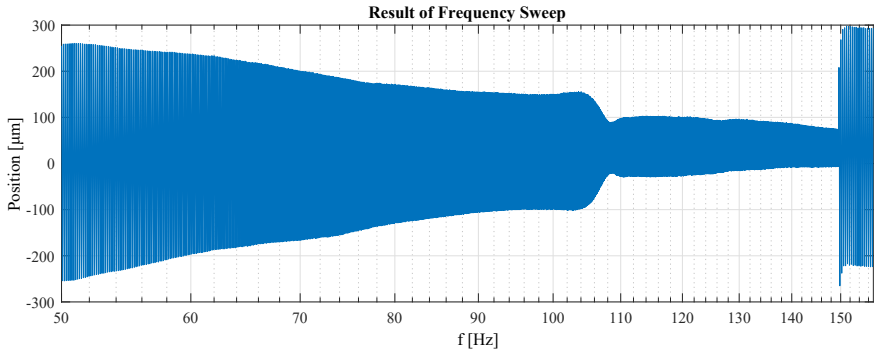

Figure 3.4: Graph showing the result of the measured position of the substrate. A frequency from $f = 50Hz$ up to $f = 150Hz$ was performed within 8 seconds. The x-axis in this figure shows the frequency that corresponds the frequency of the shaker at that time.

Furthermore, during preliminary experiments, an eigenfrequency of the shaker was found at around $f = 100Hz$. This result is shown in Fig. 3.4. According to the shaker's supplier, the device's first resonance frequency should lie above $6500Hz$. Students who have previously worked with this shaker found that another shaker frequency lies around $f = 35Hz$. The eigenfrequency here is probably a result of the 3D printed holder or the glass substrate. Therefore, all further experiments should avoid frequencies around $f = 100Hz$.

3.1.2. Volume Control and Evaporation Time

At the start of this research, an inkjet nozzle from an industrial printer was used to shoot droplets at the receptor site. This nozzle was mounted on an XY-stage capable of moving with an accuracy of approximately $5\mu m$ per incremental movement. Because of the droplets' small size, the volume deposited onto a receptor can potentially be controlled well. Fig. 3.5 shows a $2mm$ square silicon chip on which water was being deposited. This experiment shows the boundaries of Gibbs' inequality: a substantial amount of water can stay pinned at the edges since the maximum edge angle has not been overridden yet. By increasing the volume slightly with the inkjet nozzle, the size of the liquid sphere gets more extensive. Therefore, the edge angle increases until the contact line unpins and overflows.

Since the inkjet nozzle malfunctioned many times, it was not used to deposit droplets during most experiments. Instead, water was deposited onto the receptor by hand using tweezers. This method does not offer much volume control. Therefore, a solution was found to be still able to control the volume between receptor and chip. Placing a chip on top of a droplet forms an RDC configuration. By looking at the live image of the front view camera, the height of the water layer was measured with a digital calibrated ruler. By assuming straight edges of the meniscus between the receptor and chip, the volume can be approximated by calculating the volume of a cuboid.

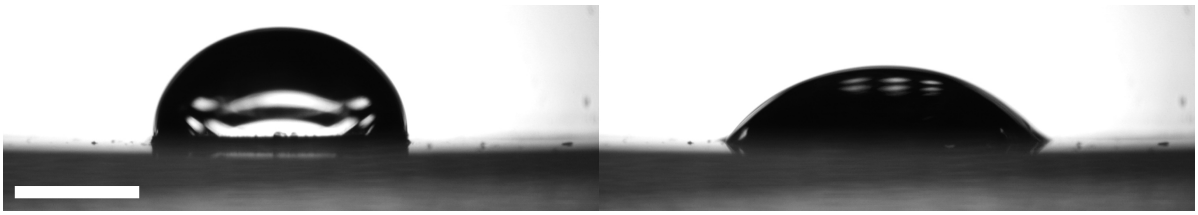

Figure 3.5: Two pictures showing a front view of a $2mm$ square silicon chip with water on top. Picture on the left is just before unpinning occurs. Picture on the right shows the overflown situation. Scale bar = $1mm$.

The evaporation time of the droplets varied significantly for different chip sizes. Relatively large volumes on 2mm chips ($V \approx 1\mu L$) evaporated in approximately 5 minutes. For $1mm$ sizes chips ($V \approx 0.1\mu L$), this time decreased to roughly 2 minutes. For chips of $L = 150\mu m$ the droplets ($V \approx 0.8nL$)) even evaporated in about 25 seconds. However, when a chip is deposited on top, minimizing the surface exposed to the ambient air drastically, the evaporation time increases significantly. In the case of a $L = 2mm$ chip, the evaporation time

of the entire lubricant film increased from 5 to approximately 25 minutes. For industrial applications, it could be relevant to look at DMSO or mixtures of water and glycerol to increase the evaporation time.

3.1.3. Chip Placement and Re-positioning

During all experiments, chips were placed by hand with a pair of tweezers. Every chip was released a few millimetres above the receptor and captured by the droplet. In most cases, the chip touches the droplet in a significantly tilted position or relatively far away from the receptor's centre. After the liquid touches the chip, it was mostly still able to align the chip well. Fig. 3.6 shows three pictures of the chip placement. Often, the chip was positioned in a (slightly) tilted pose. According to a previous study and confirmed experimentally, it is possible to re-position the system to a horizontally aligned position [42]. If the liquid volume is large enough, vibrating the system at a specific frequency will force the chip to leave its tilted pose. After the vibrations have stopped, the chip is often positioned horizontally.

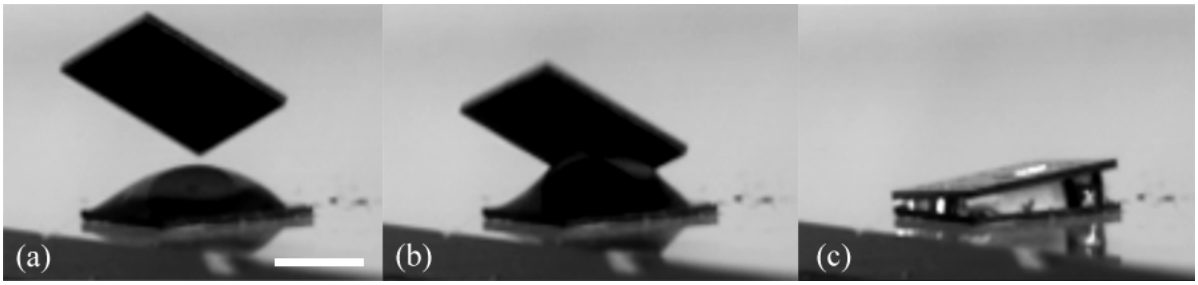

Figure 3.6: Three pictures of the capture of a $1mm$ sized chip by a liquid droplet. (a) Chip in freefall. (b) Droplet starts to touch the chip. (c) Final (tilted) position. Scale bar = $500\mu m$.

3.1.4. Component Types and Surface Treatment

All experiments have been performed with thin square silicon microchips from the same wafer, all with a thickness of $th = 50\mu m$. Chips with side lengths of $L = 2mm$ and $L = 1mm$ have been used. In Section 2.2 the assumption was made that the edges of the chips are $\phi = 90^o$. Two samples of the desired chip sizes from the wafer were taken and investigated under the scanning electron microscope (SEM), as seen Fig. 3.7. The pictures show that the $1mm$ sized chip has straight edges without much jaggedness. However, a chunk is missing from the edge, probably due to tweezer handling. The picture of the 2mm chip reveals rougher edges.

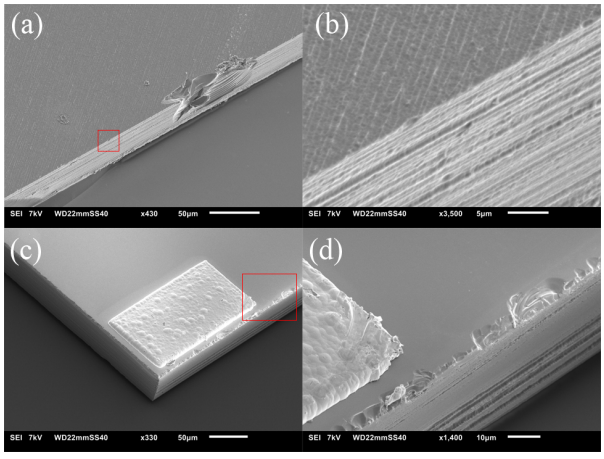

Figure 3.7: Figure (a) shows an SEM image of one of the edges of a $1mm$ square silicon chip. The red rectangle indicates what part is magnified and is shown in (b). Bottom figures (c) and (d) are SEM images of a 2mm square silicon chip. Again, the red rectangle on the left shows what part is magnified and shown in (d).

Plasma cleaning is a treatment capable of influencing the contact angle of water on solid surfaces. An advantage of using this is that the chance of facing contaminants decreases, and the contact angle is more or less equivalent in every experiment. A comparison between the contact angle before and after plasma treatment is shown in Fig. 3.8. The pictures show that the surface after treatment has become much more

hydrophilic, decreasing the contact angle significantly. However, this does mean that the maximum edge angle at which overflow occurs also decreases. This was a disadvantage for the chip placement because it was more challenging to form an RDC system successfully. Instead, chips were replaced more often and we accepted the presence of contaminants and variations in wettability properties. The surface stuck to the wafer tape was always facing towards the liquid. Also, the surfaces were cleaned with ethanol in between tests.

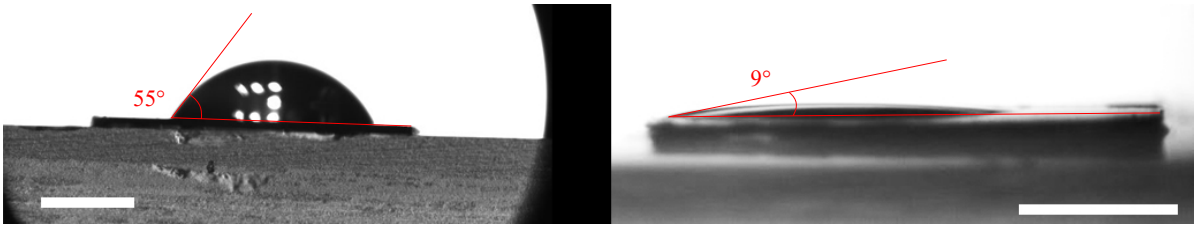

Figure 3.8: Contact angle before (left) and after plasma treatment (right). Scale bar = 500μm.

3.1.5. Observation with Tracking Algorithm

Two high-speed cameras observed the chip's displacement, after which a tracking algorithm measured the exact position in every frame. The algorithm is a point tracker using the Kanade-Lucas-Tomasi feature-tracking algorithm, which is built-in in MATLAB [12]. In the first frame, all four desired corners are detected. The next frame finds the same corners within a chosen region of interest. Doing this for all frames allows for calculating the lateral and vertical shift between receptor and chip. Since chip sizes are known, the positions of the corners also allow for the calibration of the algorithm.

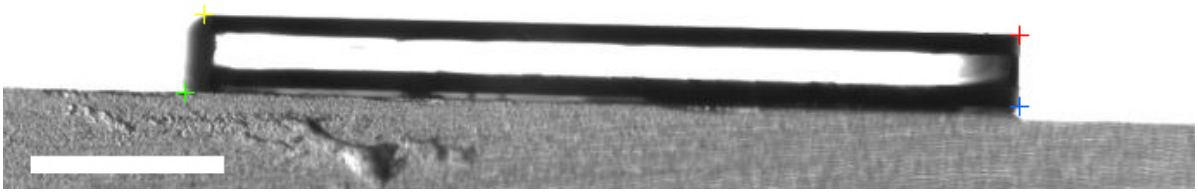

Figure 3.9: Screenshot of the four corners found by the point tracker algorithm., indicated by the crosses in yellow, red, green and blue. Scale bar = 500μm.

Measuring the positions of all corners directly from the camera frame still contains a small error. In this case, the substrate is assumed to be moving in a perfect horizontal direction. However, in reality, the substrate is always moving in a slightly tiled position. Therefore, the measured lateral and vertical displacement will always be slightly different. The error is much smaller than lateral displacement and can therefore be neglected. However, for the vertical displacement, this error is significant. The graphs in Fig. 3.10 show the difference in the measured vertical position of one of the corners of a chip. The results on the left show a sinusoidal movement just before and after the accelerations. Moreover, during the 30-period lasting accelerations, the shift moves in a sinusoidal pattern. Measuring the exact vertical displacement relative to the bottom receptor eliminates these errors. Additional explanations of this is shown in Appendix D.

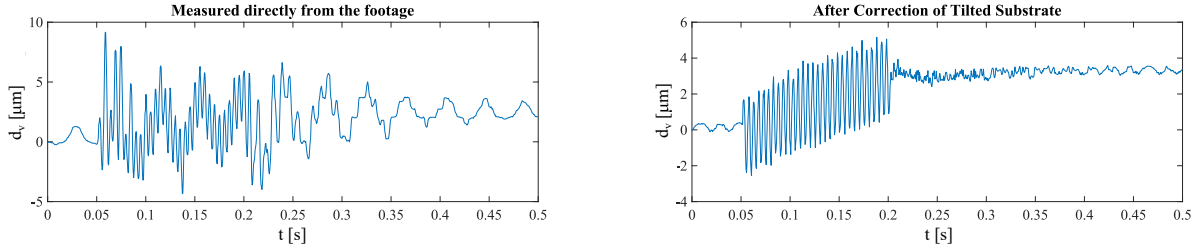

Figure 3.10: Graphs showing the difference of measuring the vertical displacement directly from the video (left), and the result after using a correction for the tilted substrate (right).

3.2. Experiments

This section describes the experiments and how these have been performed. In order to observe the existence of eigenfrequencies, frequency sweeps have been used. Not only does this answer one of the research questions, but it is also essential to do this experiment first to prevent the following experiments from being influenced by these frequencies. Next, experiments were conducted to find the effect of variables such as the chip size, water volume and acceleration magnitude. The failures and how often these occur have also been noted during all experiments.

3.2.1. Frequency Sweep

To be able to find eigenfrequencies in an RDC system, frequency sweeps have been used as a tool to find them. Using a logarithmic frequency sweep instead of a linear one, all periods of every frequency are of equal lengths. This increases the chance of finding the eigenfrequencies. Since the high-speed cameras only allow filming for a short period ($< 15s$), the first experiments were done in segments of short frequency ranges ($< 50Hz$). However, this is very time-consuming. Therefore, all following experiments were performed using longer sweeps ($= 120s$) and more significant frequency ranges ($= 100Hz$). During these tests, the oscilloscope shows at all times at what frequency the sweep is. Looking at the live image should show if the movements of the top chip increase at specific frequencies.

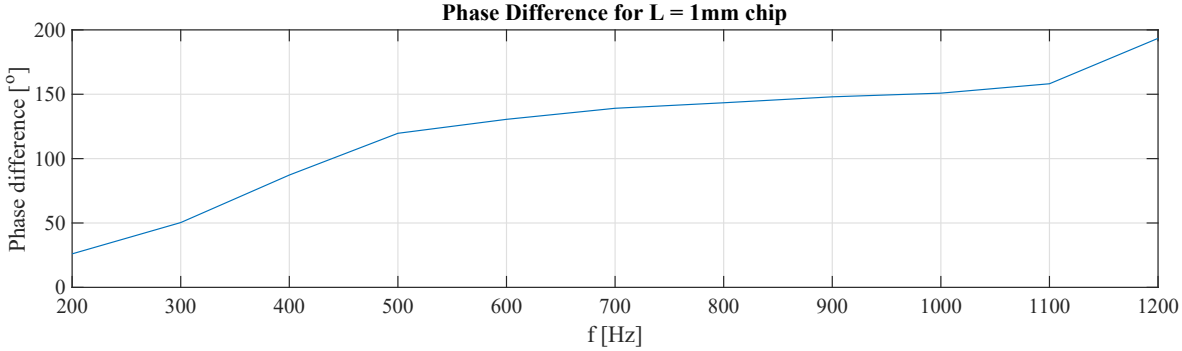

Figure 3.11: Phase diagram obtained by looking at the input (position receptor) and the output (relative shift chip) for different frequencies. A $L = 1mm$ chip has been used.

Tests were performed with chips of $L = 1mm$. After several sweeps, ranging from $f = 100Hz$ up to $f = 1200Hz$, no eigenfrequencies were observed in the live image. Therefore, several tests were done in which the input and output of the system were compared to each other. At frequencies ranging from 100 up to $1000Hz$ with steps of $100Hz$, the position of the receptor (input) and the lateral relative shift of the top chip (output) were tracked with the tracking algorithm. These results show that for an increase in frequency, the phase difference increases as well. At approximately $f = 700Hz$, the phase lag remains at around 150^o and keeps slightly increasing. Especially from $200Hz$ up to $600Hz$, the phase increases greatly from a low phase lag up to 150^o. This could indicate that halfway between these frequencies, there exists an eigenfrequency. Another indication of an eigenfrequency could be an increase in the relative shift of the chip. However, as the frequencies increase, the amplitude of the shaker drastically decreases. From $f = 1000Hz$ and higher, the lateral shift of the top chip is $x < 2\mu m$ making it difficult to observe. Therefore, it was impossible to get useful data from the magnitude plot. Future investigations should use a linear shaker that can maintain a constant amplitude for different frequencies.

3.2.2. Start-Stop Phenomena and Variation of Variables

The characteristic motion at the start, during accelerations and towards rest is investigated with experiments in this section. Here, three variables are changed to investigate their effect on these motions and their influence on failure. Experiments have been performed with two different chip sizes ($L = 1mm, L = 2mm$), a variation of lubricant layer thicknesses and different acceleration magnitudes. Since the shaker shows drift and eigenfrequencies should be avoided, all experiments here are performed at $f = 200Hz$ for 30 periods. Between all series of tests, the receptor is cleaned with ethanol and the top chip is replaced by a new one.

The first figure shows the results of a variation in lubricant height. A chip size of $L = 2mm$ has been used and all experiments have been performed at a constant acceleration of $a = 22.5g$. The results show the lateral

shift of the chip relative to the bottom receptor. As expected, an increase in lubricant height also increases the shift. This effect seems to be relatively linear with the increase in h_0. The model predicted that, for these values, the shift should increase linearly. Additional results presented in Fig. E.3, Fig. E.4 and Fig. E.5 suggest that this is indeed true.

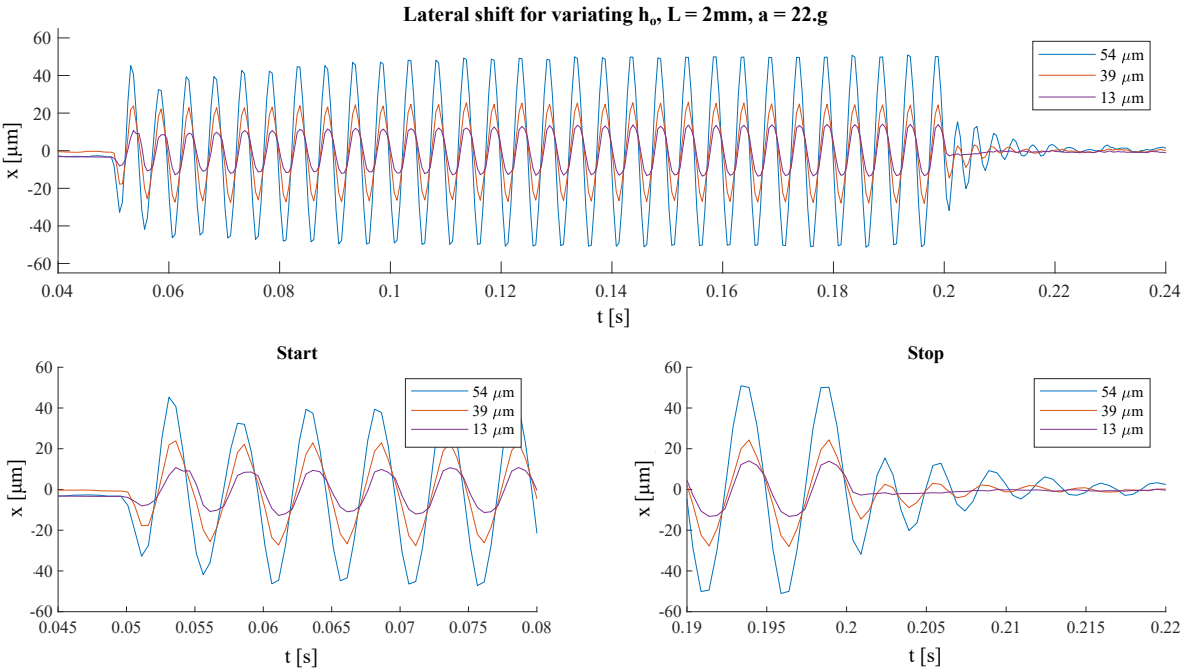

Figure 3.12: Three graphs showing the lateral shift of a $L = 2mm$ chip relative to its receptor. In all situations the acceleration was kept at $a = 22.5g$. The lubricant height varied to show its effect on the displacement. The two graphs in the bottom are a magnified plot of the top graph.

For higher lubricant heights, the system's damping in the lateral direction seems to decrease. For a thickness of $h_0 = 54\mu m$, the system requires more time to oscillate towards the equilibrium position compared to smaller thicknesses. This could be explained by looking at the viscous forces calculated in 2.4, which decreases for an increasing lubricant height. The viscous force is dependent on the relative speed between two plates (here, the receptor and chip) and can therefore be approximated as the lateral damping of the system [47]. Also, there seems to be an increase in a lateral shift during the first ± 10 periods. This corresponds to the starting behaviour of the shaker, but it cannot be concluded yet if this is the leading cause. Another reason could be that the system needs time to adjust to the movement of the shaker due to the inertial effects of both the liquid and mass of the chip.

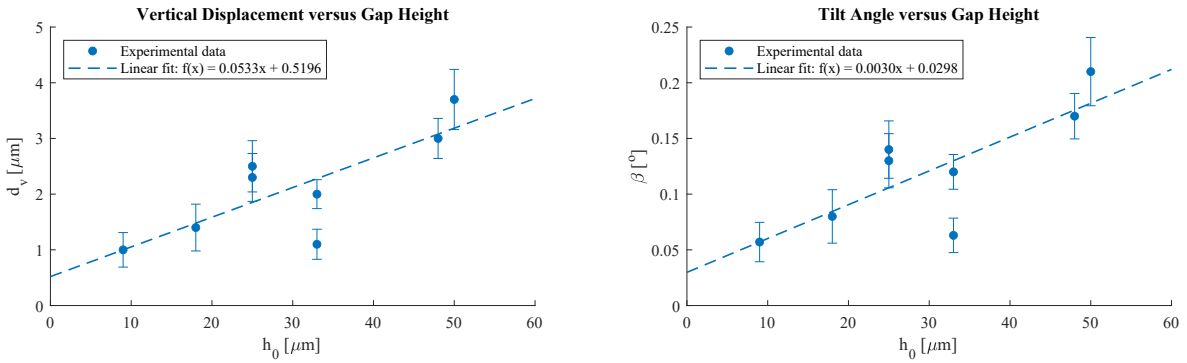

Figure 3.13: Results of the vertical shift of one of the corners of a chip (left), and the tilt angle of the chip (right). Numbers are shown for an increased value of h_0. Results are from experiments with a 2mm sized chip accelerated at 16.9g at a frequency of 200Hz. The dashed line indicates a fitted polynomial of degree 1 found with the least squares method.

The vertical shift of the corners and the chip's tilt angle have been measured as well and are shown in Fig. 3.13. These graphs show that the vertical shift and, therefore, the tilt decreases for a smaller lubricant height. When the vertical motion of the chip becomes very small, it is more difficult to measure the exact displacement. This is because of the limitations of the tracking algorithm and the number of frames that have been shot. These results could be improved by increasing the number of frames per second during filming or improving the image's contrast.

Next, the effect of changing the accelerations is investigated. The relevant figures can be found in Appendix E. As expected, increasing the acceleration magnitude increases the lateral shift of the chip as well. Note that more than doubling the acceleration ($12.1g$ compared to $22.5g$) does not result in a doubling of lateral shift. In these cases, the maximum shift increases from $\approx 37\mu m$ to $\approx 50\mu m$. The model from Sec. 2.3 predicted that the shift should increase linearly for an increase of accelerations up to $a = 40g$. However, it seems that the shift already increases non-linearly at lower accelerations.

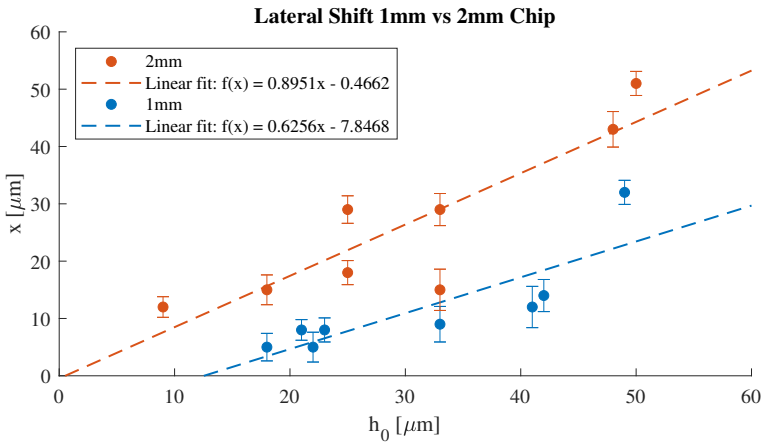

Figure 3.14: Scatter plot of the difference between the lateral shift in case of a 1mm and 2mm chip. Error bars originate from the mean displacement of the top left and right corner, and the resolution of the camera. The dashed lines indicate the trend of both results. The dashed line indicates a fitted polynomial of degree 1 found with the least squares method.

The last variable that has been investigated is the chip length L. Several experiments with fixed lubricant heights have been performed to find its effect on the lateral shift. Fig. 3.14 shows the results of the shift of a $1mm$ chip and a $2mm$ chip at equal accelerations. It shows that a smaller chip size results in a decrease in the shift. This does not directly mean that this is because the mass of the chip has decreased. A smaller chip also results in a smaller volume of water between the receptor and chip, decreasing the inertial effects of the liquid. Future research could focus on making the chip lengths dimensionless to find out if the shift is decreasing linearly with a decrease in chip size.

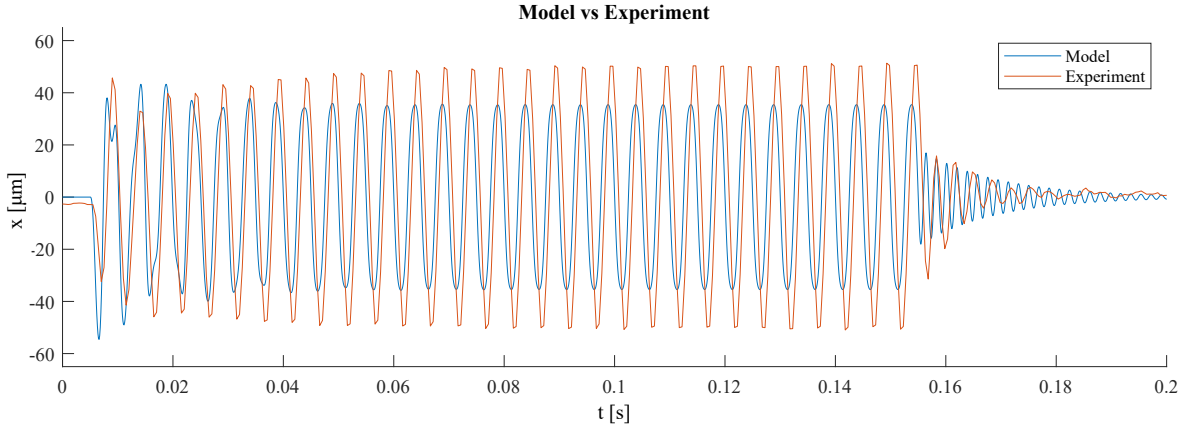

Figure 3.15: Two plots showing a comparison between the non-linear model describing only shift (blue) with one of the experiments (red). Both the model and experiment were executed at a frequency of $f = 200Hz$ for 30 periods, acceleration of $a = 22.5g$ and a lubricant height of $h_0 = 54\mu m$.

The shift predicted by the non-linear model described in the previous chapter is compared to experimental data. One example of this comparison is shown in Fig. 3.15. Here, in both situations, a chip of 2mm has been accelerated up to $22.5g$ for a total of 30 periods at $200Hz$. The lubricant height in both situations was $h_0 = 54\mu m$. The motions of both experiment and the model follow each other in several ways. A visualization of this can also be found in Appendix E. Both graphs show a similar sinusoidal motion for all 30 periods, and they both require approximately 0.025 seconds to oscillate to their equilibrium position after the accelerations have stopped. Compared to other experiments with different values for h_0, L and a, these equalities are also valid. However, there are some differences too. During most experiments, the time required to oscillate towards the equilibrium position is much shorter than in the model. This could be explained by higher damping of the meniscus in reality. Many assumptions have been made regarding the liquid bridge. For instance, the inertial effects of the liquid have been neglected, and the shape of the meniscus has been assumed to have straight edges all the time. Another difference is the measured lateral displacement compared to the predicted shift. In Fig. 3.15, the difference in peak displacement measures a total of $15\mu m$. This can also be explained by all the assumptions made in the model. Also, the measurements have a certain amount of error. For instance, the lubricant height has been measured with a digital ruler, possibly resulting in an error of several microns. The model also assumes that the receptor and chip are perfectly shaped rectangles with smooth surfaces and sharp edges. While in reality, this is not the case as was described in Sec. 3.1.4. Additionally, the model shows some extra peaks and a significant dip at the starting motion. This could be due to the sensitivity of the non-linear equation.

3.3. Stability Region

During all experiments described in the previous subsections, situations in which unpinning occurred have also been noted. These results, combined with the predictions made in Chapter 2, provide a region where the RDC should remain intact after accelerating. The models and theory predicted that the contact lines should be unpinning if the edge angles exceed specific boundary values. This results in overflow and misalignment of the chip. Theoretically, it should be impossible that dry friction occurs due to the tilting of the chip. A scatter plot in Fig. 3.16 shows the number of failed versus successfully performed experiments. Here, success means that the RDC configuration is still intact after accelerating. A chip size of $L = 2mm$ has been used in these tests.

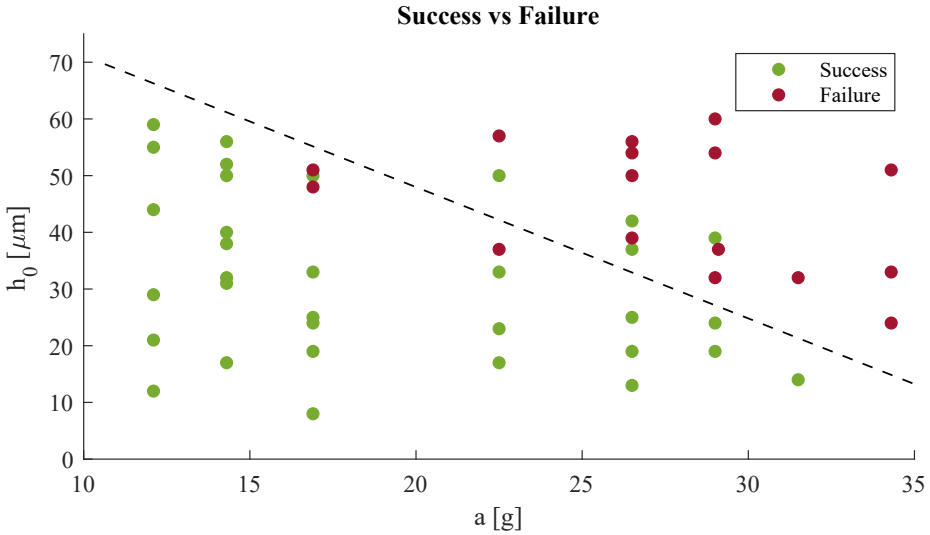

Figure 3.16: Scatter plot showing the results of experiments that resulted in success versus failure. Here, success means that the RDC configuration is still intact after it has accelerated for a total of 30 periods. Otherwise, the system has failed. The black dashed line represents the position at which most successes seem to transition into failure. All experiments have been performed with 2mm sized chips with a variation in lubricant height and acceleration magnitude.

In general, the results show that larger values of h_0 and a result in a higher chance of failure. There seems to be a decreasing trend in the chance of success, corresponding to an increase in acceleration for constant values of h_0. In some cases, the experiments have resulted in unpinning, where the RDC remained intact for equivalent accelerations but with larger gaps. The variation between the experiments can explain this. The

contact angle strongly affects the boundary limits of pinned contact lines and deviated with $\pm 5^o$ between tests. Other explanations could be unwanted contaminants, damaged edges or misalignment and tilt of the chip at the beginning of the experiment. Based on these results, finding the exact boundaries of a region in which the RDC will remain stable is not possible. However, it does give an idea of where this region probably lies.

$a\,[g]$	$h_0\,[\mu m]$	$x[\mu m]$	$\theta_0\,[^o]$	$\theta_{max}\,[^o]$	$\theta_{min}\,[^o]$
16.9	48	23	51	NA	NA
16.9	51	36	52	162	19
22.5	50	68	58	167	12
22.5	54	59	56	NA	NA
32	37	87	54	171	8

Table 3.1: Overview of the failure conditions in terms of acceleration a, lubricant height h_0, lateral shift x, measured contact angle θ_0, and the maximum and minimum edge angles. NA means that the data was not available.

Not all experiments failed after exactly 30 periods. An example of the shift of a chip during failure can be seen in Fig. 3.18. The red box in these figures indicates the moment at which unpinning of one of the contact lines occurs. In the left graph, a constant oscillating shift is suddenly interrupted by a higher peak, after which the shift increases significantly. The tilting angle on the right does not show any noticeable movements. Other experiments confirm the behaviour observed in these graphs as well. The parameters and measured results of several tests that failed are summarised in Table 3.1. The lateral shift shown in this table is the maximum value the chip reached in the period before unpinning occurred. Since not all videos captured the actual unpinning of the meniscus, it is difficult to say at what exact values the unpinning occurred. However, what is noticeable from this data, are the maximum and minimum values that the edge angles have reached before unpinning. Note that after these values were reached, the system was still intact. Theoretically, the contact lines should have unpinned at values just below the contact angle θ_0 and above $\theta_0 + 90^o$. If only one of these values had been exceeded, it could be explained by an error in the measured contact angle. Another explanation could be found in the assumption that all surfaces are approached as straight lines. Perhaps, the liquid surfaces are differently shaped during large displacements. Future work could focus on explaining this.

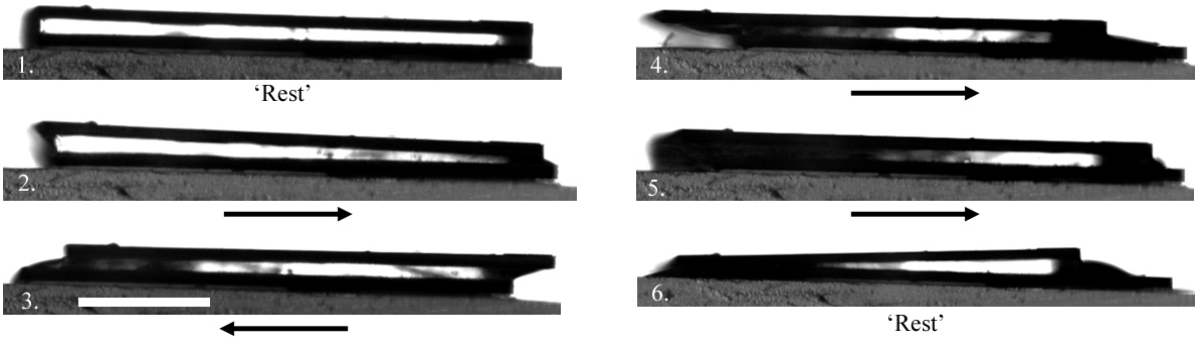

Figure 3.17: Six screenshots showing the motion of a 2mm chip on a liquid with $h_0 = 37\mu m$ accelerated with $a = 32g$. 1) The system at rest 2) 3) Shaker starts accelerating to the right and left. 4) Contact line at the bottom right starts to unpin. 5) Liquid starts overflowing on the right. 6) Failed configuration.

Some critical moments during the motion of a chip before, during, and after unpinning of the contact line have been captured. This footage's screenshots are shown in Fig. 3.17. Six steps are shown from the starting 'rest' position up until failure. The arrows indicate the direction the substrate and receptor are moving in. An important detail can be seen in step four. At the bottom right, unpinning of the contact line is visible. Immediately after this line has unpinned, the lateral shift increases significantly, and the liquid starts overflowing on the left side. Once that happens, the system cannot re-align and finally, 6) dry friction between the top chip and bottom receptor prevents the system from moving. From this perspective, the overflow only happens at the left edge. The second camera, filming from the side, confirms that in all cases, the liquid only overflows at one side of the edges once it happens.

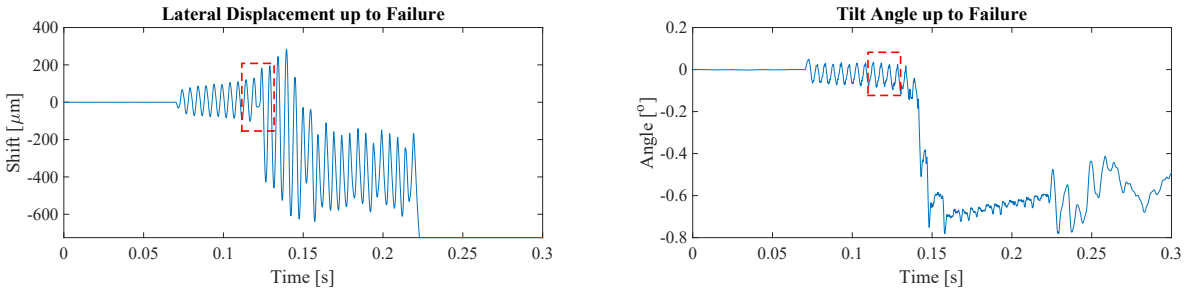

Figure 3.18: Two graphs showing the lateral displacement and tilt angle of the chip shown in Fig. 3.17. The red box indicates the moment at which one of the contact lines unpins.

For values of the gap height smaller than $h_0 < 10\mu m$, the component shift shows different results. Results of this are given in Appendix E. The chip keeps moving sinusoidally in both lateral directions, but rapid movements occur at the peak displacements. This happens in most experiments, and this behaviour strongly increases when the gap height decreases below $h_0 = 10\mu m$. A possible explanation could be the camera's resolution of approximately $1.5\mu m$. Another explanation could be the existence of dry friction. On the captured images, it is difficult to see if the chip and receptor physically touch. Therefore, this cannot be confirmed. As mentioned in section 2.5, other experiments did observe this and recommended using a minimum volume to prevent dry friction.

Combining the results from Chapter 2 with the found results here approximates a stability region for a 2mm sized chip. The plot in Fig. 3.19 indicates with red combinations of h_0 and a, which will most likely result in misalignment, tilted positions of the chip, dry friction or unpinning of the contact lines. The green area represents combinations of h_0 and a, likely to maintain the RDC after accelerations. The red dashed line shows the combinations of a and h_0 at which unpinning occurs according to the model. The black dashed line indicates when most of the unpinning occurred based on experimental results. This difference can be explained by a variance in contact angle between the experiments, impurities of the chip's and receptor's edges or unwanted contaminants. Also, the black dashed line is less steep than the red line. This could be explained by the lack of constraining the maximum water volume in the model. Too much liquid can result in a tilted pose of the chip, or the extra mass of the liquid could play a more significant role in the movements of liquid and chip, making the system more unstable. Finally, the blue dashed line represents the boundary at which the chance on dry friction increases significantly. The found results from the experiments only indicate that this likely happens but cannot confirm it. However, the results combined with experience and data from similar investigations are convincing enough to set this boundary.

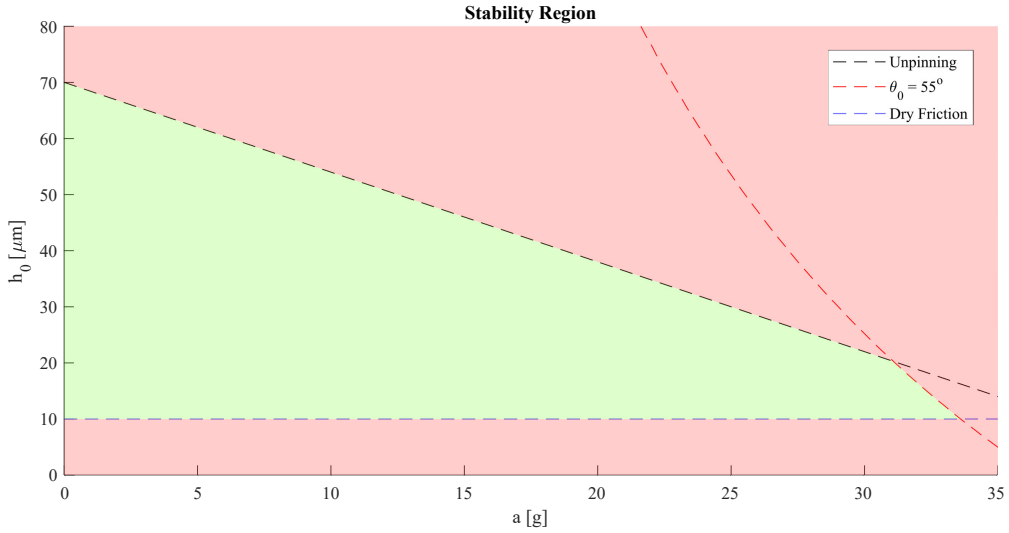

Figure 3.19: Stability region based on models, experimental results and literature. Red surface represents combinations of h_0 and a which most likely result in unpinning of the contact lines, misalignment or tilted pose of the chip or dry friction. The green area shows combinations of h_0 and a resulting in maintaining an intact RDC. The results are based on $L = 2mm$ chips and $\theta_0 = 55^o$.

4

Conclusion and Recommendations

This research explains how capillary interfaces can contain and align small components subjected to high accelerations. Two models predict how an RDC configuration will behave when the receptor is accelerating and were compared to outcomes from an experimental setup. Up to now, research mainly has focussed on static situations rather than a moving system. This investigation shows the results of a dynamic situation and explains where the stability limits of such a system lie. As stated before, this study answers the following research question:

"What are the limits to the alignment capabilities of a liquid bridge between receptor and component subject to high accelerations?"

Failure Modes

One of the sub-questions supporting the main research questions is: "*What failure modes do exist that disrupt the liquid bridge and what causes these to happen?*". This study predicts and observes two failure modes: unpinning of the contact lines and dry friction. A contact line unpins when the edge angles of the meniscus are small or large enough. These boundaries are given by Gibbs' inequality condition, which strongly depends on the contact angle of the liquid and the topological edge angle of the solid. When a contact line unpins, the meniscus starts to overflow, disrupting the liquid bridge and making it impossible for the system to re-align.

If the contact angle on the solid surface changes, the maximum and minimum values for the advancing and receding angles also change. Maximising these stability boundaries requires the advancing angle to be as small and the receding angle as large as possible. However, no treatment or solution yet exists that can provide both. There is always a trade-off between these values. Therefore, a contact angle of $\theta_0 = 45^o$ is a compromise maximising the stability limits in the case of a solid edge of $\phi = 90^o$. The other failure mode occurs when the top component is in contact with the bottom receptor and cannot move due to dry friction. Here, the system is not able to re-align either.

Modelling the System

The second sub-question is: "*How can the lateral displacement and tilting of the component during accelerations be modelled?*". This study shows a non-linear model based on the minimisation of surface energy to predict the lateral shift relative to the receptor. Surface Evolver, a computational software, validated the model's stiffness and shows that this element is very accurate. A second model based on squeeze flow theorem uses the first model's results and predicts the chip's vertical motions and tilt. Tough the model is non-linear, the results show that for values up to $h_0 = 30\mu m$, $a = 40g$ and $L = 1mm$ the system behaves rather linear. Both models indicate that a decrease in variables such as lubricant height, acceleration magnitude and chip dimensions decrease the resulting displacements. Here, the lubricant height affects the displacements the most and can therefore be seen as the most important variable.

An experimental setup with high-speed cameras and rectangular chips of $L = 1mm$ and $L = 2mm$ combined with water as a lubricant has been used. A well-working tracking algorithm with high resolution obtained all shown results. The experiments confirm the trends and behaviour of the variables as predicted

in the models. For lower values, the relative displacements decreased, and the results show linear trends. Smaller lubricant heights and chip sizes result in reduced lateral and vertical displacements. Also, for the first time tilt of a chip during accelerations has been captured. The experiments show that for smaller values of the variables, the tilt angle also decreases. Simulated motions of the top chip during oscillating accelerations show a similar pattern to the experiment.

However, the experimental results' magnitudes show some differences compared to the models. These can be explained by looking at the assumptions made at the beginning of every model. Moreover, environmental conditions and better control of liquid volume and component deposition could improve the results.

Eigenmodes

The experiments also give new insight into the existence of eigenfrequencies. Chips of $L = 1mm$ show that at some frequencies, the relative displacement increases and that the system is moving more out of phase. This might indicate that close to these frequencies, eigenmodes exist, affecting the movements of the chip and meniscus. The models do not describe these, and experiments only show that they are possibly there. Future research could focus more on predicting and observing the existence of these eigenfrequencies. Using a shaker that provides a constant magnitude and liquids evaporating slower could be helpful in such experiments.

Stability Region

The third supporting sub-question is: "*What methods exist to predict when a component is lost during transport due to accelerations?*". Based on the models, a descending trend exists representing combinations of a and h_0 resulting in the maximum possible edge angles during accelerations. According to this, chips of $L = 2mm$ should be able to accelerate up to $a = 45g$ without unpinning. The model also suggests that it is crucial to include tilting effects since these also influence the edge angles. The experiments revealed that chips of these sizes unpin at lower accelerations and smaller lubricant height values than the model. The reason why there is no clear boundary in the experimental results can be explained by a variation in contact angle between the experiments, unwanted contaminants or damaged edges. Also, the system unpinned for relatively high lubricant heights at smaller accelerations. This can be explained by the lack of constraining the maximum volume of water in the model. Too large volumes of liquid may result in a tilted pose of the chip or a significantly moving mass of water, making the RDC system unstable. Future research could focus on implementing these concepts into a model to make it more conservative. For smaller chip sizes of $L = 1mm$, the RDC configuration remained repeatedly intact for accelerations up to $a = 35g$. This result confirms that the system is more stable for smaller chip sizes. Future studies could focus on decreasing the chip size and finding stability limits at even higher accelerations. This study shows that capillary interfaces can handle and transport small parts at very high accelerations under the right conditions. Therefore, this technique seems very promising to integrate into high dynamics transport machines.

Bibliography

[1] Fortune Business Insights, 2022. URL https://www.globenewswire.com/en/news-release/2022/05/02/2433410/0/en/With-9-2-CAGR-Semiconductor-Market-Size-worth-USD-893-10-Billion-in-2029.html.

[2] Global Semiconductor Sales, Units Shipped Reach All-Time Highs in 2021 as Industry Ramps Up Production Amid Shortage, 2022. URL https://www.semiconductors.org/global-semiconductor-sales-units-shipped-reach-all-time-highs-in-2021-as-industry-ramps-up-produc

[3] G. Arutinov, E. C. P. Smits, P. Albert, P. Lambert, and M. Mastrangeli. In-plane mode dynamics Supporting Information. pages 1–12.

[4] J. Berthier, K. A. Brakke, S. Mermoz, C. Frétigny, and L. Di Cioccio. Stabilization of the tilt motion during capillary self-alignment of rectangular chips. *Sensors and Actuators, A: Physical*, 234:180–187, 2015. ISSN 09244247. doi: 10.1016/j.sna.2015.09.008. URL http://dx.doi.org/10.1016/j.sna.2015.09.008.

[5] S. Biswas, M. Mozafari, T. Stauden, and H. O. Jacobs. Surface tension directed fluidic self-assembly of semiconductor chips across length scales and material boundaries. *Micromachines*, 7(4), 2016. ISSN 2072666X. doi: 10.3390/mi7040054.

[6] K. A. Brakke. Surface Evolver, 1992.

[7] Adam Chafa, Engineering Sciences, and Pierre Lambert. High Dynamics Capillary Gripping and Transport of Micro-Objects. 2022.

[8] B. Chang, A. Shah, Q. Zhou, R. H.A. Ras, and K. Hjort. Self-transport and self-alignment of microchips using microscopic rain. *Scientific Reports*, 5:1–8, 2015. ISSN 20452322. doi: 10.1038/srep14966.

[9] B. Chang, Z. Zhu, M. Koverola, and Q. Zhou. Laser-assisted mist capillary self-alignment. *Micromachines*, 8(12):1–10, 2017. ISSN 2072666X. doi: 10.3390/mi8120361.

[10] S. Cho, D. Lee, and S. Kwon. Fluidic self-assembly transfer technology for micro-led display. *2019 20th International Conference on Solid-State Sensors, Actuators and Microsystems & Eurosensors XXXIII (TRANSDUCERS & EUROSENSORS XXXIII)*, (June):402–404, 2019.

[11] N. B. Crane, O. Onen, J. Carballo, Q. Ni, and R. Guldiken. Fluidic assembly at the microscale: Progress and prospects. *Microfluidics and Nanofluidics*, 14(3-4):383–419, 2013. ISSN 16134990. doi: 10.1007/s10404-012-1060-1.

[12] Lucas D., Bruce, and Takeo Kanade. An Iterative Image Registration Technique with an Application to Stereo Vision. *Proceedings of the 7th International Joint Conference on Artificial Intelligence*, pages 674–679.

[13] V. Dubey, E. Beyne, J. Derakhshandeh, and I. De Wolf. Physics of self-aligned assembly at room temperature. *Physics of Fluids*, 30(1), 2018. ISSN 10897666. doi: 10.1063/1.5004797.

[14] Jan Engmann, Colin Servais, and Adam S. Burbidge. Squeeze flow theory and applications to rheometry: A review. *Journal of Non-Newtonian Fluid Mechanics*, 132(1-3):1–27, 2005. ISSN 03770257. doi: 10.1016/j.jnnfm.2005.08.007.

[15] J. Fang and K. F. Böhringer. High yield batch packaging of micro devices with uniquely orienting self-assembly. *Proceedings of the IEEE International Conference on Micro Electro Mechanical Systems (MEMS)*, (January 2005):12–15, 2005. ISSN 10846999. doi: 10.1109/memsys.2005.1453855.

[16] J. Fang and K. F. Böhringer. Parallel micro component-to-substrate assembly with controlled poses and high surface coverage. *Journal of Micromechanics and Microengineering*, 16(4):721–730, 2006. ISSN 09601317. doi: 10.1088/0960-1317/16/4/008.

[17] Gualtiero Fantoni, Marco Santochi, Gino Dini, Kirsten Tracht, Bernd Scholz-Reiter, Juergen Fleischer, Terje Kristoffer Lien, Guenther Seliger, Gunther Reinhart, Joerg Franke, Hans Nørgaard Hansen, and Alexander Verl. Grasping devices and methods in automated production processes. *CIRP Annals - Manufacturing Technology*, 63(2):679–701, 2014. ISSN 17260604. doi: 10.1016/j.cirp.2014.05.006. URL `http://dx.doi.org/10.1016/j.cirp.2014.05.006`.

[18] T. Fukushima, E. Iwata, Y. Ohara, M. Murugesan, J. Bea, K. Lee, T. Tanaka, and M. Koyanagi. Multichip self-assembly technology for advanced die-to-wafer 3-D integration to precisely align known good dies in batch processing. *IEEE Transactions on Components, Packaging and Manufacturing Technology*, 1 (12):1873–1884, 2011. ISSN 21563950. doi: 10.1109/TCPMT.2011.2160266.

[19] D. Grier. A revolution in optical manipulation. *Nature*, (424):810–816, 2003. doi: https://doi.org/10.1038/nature01935.

[20] Xinling Wang Haiyan Jia, Erik Mailand, Jiangtao Zhou, Zhangjun Huang, Giovanni Dietler, John M. Kolinski. Universal Soft Robotic Microgripper. *Small*, 15(4), 2018. doi: https://doi.org/10.1002/smll.201803870.

[21] H. O. Jacobs, A. R. Tao, A. Schwartz, D. H. Gracias, and G. M. Whitesides. Fabrication of a cylindrical display by patterned assembly. *Science*, 296(5566):323–325, 2002. ISSN 00368075. doi: 10.1126/science.1069153.

[22] Masayuki Kaneda, Michinori Yamamoto, Koichi Nakaso, Tsuyoshi Yamamoto, and Jun Fukai. Oscillation of a tilted circular pad on a droplet for the self-alignment process. *Precision Engineering*, 31(2):177–184, 2007. ISSN 01416359. doi: 10.1016/j.precisioneng.2006.03.005.

[23] R. J. Knuesel and H. O. Jacobs. Self-assembly of microscopic chiplets at a liquid - Liquid - solid interface forming a flexible segmented monocrystalline solar cell. *Proceedings of the National Academy of Sciences of the United States of America*, 107(3):993–998, 2010. ISSN 00278424. doi: 10.1073/pnas.0909482107.

[24] P. Lambert and S. Régnier. Surface and contact forces models within the framework of microassembly. *Journal of Micromechatronics*, 3(2):123–157, 2006. ISSN 13892258. doi: 10.1163/156856306777544970.

[25] P. Lambert, M. Mastrangeli, J. B. Valsamis, and G. Degrez. Spectral analysis and experimental study of lateral capillary dynamics for flip-chip applications. *Microfluidics and Nanofluidics*, 9(4-5):797–807, 2010. ISSN 16134982. doi: 10.1007/s10404-010-0595-2.

[26] S. J. Lee, M. M. Denn, M. J. Crochet, and A. B. Metzner. Compressive flow between parallel disks:. I. Newtonian fluid with a transverse viscosity gradient. *Journal of Non-Newtonian Fluid Mechanics*, 10 (1-2):3–30, 1982. ISSN 03770257. doi: 10.1016/0377-0257(82)85002-7.

[27] I. Martinez, J. M. Perales, and J. Meseguer. Non-linear response of a liquid bridge to a sinusoidal acceleration under microgravity. *Experiments in Fluids*, 37(6):775–781, 2004. ISSN 07234864. doi: 10.1007/s00348-004-0837-8.

[28] M. Mastrangeli, S. Abbasi, C. Varel, C. Van Hoof, J. P. Celis, and K. F. Böhringer. Self-assembly from milli- to nanoscales: Methods and applications. *Journal of Micromechanics and Microengineering*, 19(8), 2009. ISSN 09601317. doi: 10.1088/0960-1317/19/8/083001.

[29] M. Mastrangeli, Q. Zhou, V. Sariola, and P. Lambert. Surface tension-driven self-alignment. *Soft Matter*, 13(2):304–327, 2017. ISSN 17446848. doi: 10.1039/c6sm02078j.

[30] Massimo Mastrangeli, Gari Arutinov, Edsger C.P. Smits, and Pierre Lambert. Modeling capillary forces for large displacements. *Microfluidics and Nanofluidics*, 18(4):695–708, 2015. ISSN 16134990. doi: 10.1007/s10404-014-1469-9.

[31] J. Meseguer, L. A. Slobozhanin, and J. M. Perales. A review on the stability of liquid bridges. *Advances in Space Research*, 16(7):5–14, 1995. ISSN 02731177. doi: 10.1016/0273-1177(95)00126-Y.

[32] J. Meseguer, J. L. Espino, A. Cuerva, and A. Sanz-Andrés. Minimum volume of long liquid bridges between noncoaxial, nonequal diameter circular disks under lateral acceleration. *Physics of Fluids*, 17(10), 2005. ISSN 10706631. doi: 10.1063/1.2107747.

[33] K. S. Park, X. Xiong, R. Baskaran, and K. F. Böhringer. Fluidic self-assembly of millimeter scale thin parts on preprogrammed substrate at air-water interface. *Proceedings of the IEEE International Conference on Micro Electro Mechanical Systems (MEMS)*, (December 2013):504–507, 2010. ISSN 10846999. doi: 10.1109/MEMSYS.2010.5442454.

[34] K. S. Park, J. H. Hoo, R. Baskaran, and K. F. Böhringer. Orientation-controlled parallel assembly at the air-water interface. *Journal of Micromechanics and Microengineering*, 22(10), 2012. ISSN 09601317. doi: 10.1088/0960-1317/22/10/105028.

[35] Kwang Soon Park, Ji Hao Hoo, Rajashree Baskaran, and Karl F. Böhringer. Optimization of angular alignment in self-assembly of thin parts at an air-water interface. *Journal of Microelectromechanical Systems*, 22(1):13–15, 2013. ISSN 10577157. doi: 10.1109/JMEMS.2012.2231052.

[36] M. Park, C. Lee, and J. Hong. Phase transitions and critical phenomena in the liquid bridge under lateral acceleration. *Physical Review E - Statistical Physics, Plasmas, Fluids, and Related Interdisciplinary Topics*, 64(2):4, 2001. ISSN 1063651X. doi: 10.1103/PhysRevE.64.027302.

[37] S. C. Park, J. Fang, S. Biswas, M. Mozafari, T. Stauden, and H. O. Jacobs. A First Implementation of an Automated Reel-to-Reel Fluidic Self-Assembly Machine. *Advanced Materials*, 26(34):5942–5949, 2014. ISSN 15214095. doi: 10.1002/adma.201401573.

[38] J. M. Perales, J. Meseguer, and I. Martínez. Minimum volume stability limits for axisymmetric liquid bridges subject to steady axial acceleration. *Journal of Crystal Growth*, 110(4):855–861, 1991. ISSN 00220248. doi: 10.1016/0022-0248(91)90643-J.

[39] V. Sariola, Q. Zhou, R. Laaß, and H. N. Koivo. Experimental study on droplet based hybrid microhandling using high speed camera. *2008 IEEE/RSJ International Conference on Intelligent Robots and Systems, IROS*, pages 919–924, 2008. doi: 10.1109/IROS.2008.4651009.

[40] V. Sariola, M. Jääskelinen, and Q. Zhou. Hybrid microassembly combining robotics and water droplet self-alignment. *IEEE Transactions on Robotics*, 26(6):965–977, 2010. ISSN 15523098. doi: 10.1109/TRO.2010.2066830.

[41] K. Sato, K. Ito, S. Hata, and A. Shimokohbe. Erratum: Self-alignment of microparts using liquid surface tension - Behavior of micropart and alignment characteristics (Precision Engineering (2003) 27 (42-50) PII: S0141635902001824). *Precision Engineering*, 27(4):444, 2003. ISSN 01416359. doi: 10.1016/S0141-6359(03)00007-2.

[42] K.L. Scott, R.T. Howe, and C.J. Radke. Model for micropart planarization in capillary-based microassembly. *Transducers*, pages 1319–1322, 2003.

[43] Daewon Lee Seongkyu Cho, Wonseok Choi, Sunghoon Han, Junhoi Kim, Amos C. Lee, Su Deok Kim, Seo Woo Song, Changsoon Kim. Micro-Concentrator Photovoltaics Using Fluidic Self-Assembly Technology. *Wiley*, 6(12), 2021. doi: https://doi.org/10.1002/admt.202100312.

[44] S. Skink. *Encyclopedia of Nanotechnology*. 2012. ISBN 9789048197514. doi: 10.1007/978-90-481-9751-4.

[45] T. Srinivasan, D. Liepmann, and R. T. Howe. Microstructure to substrate self-assembly using capillary forces. *Journal of Microelectromechanical Systems*, 10(1):17–24, 2001. ISSN 10577157. doi: 10.1109/84.911087.

[46] C. G. Tsai, C. M. Hsieh, and J. A. Yeh. Self-alignment of microchips using surface tension and solid edge. *Sensors and Actuators, A: Physical*, 139(1-2 SPEC. ISS.):343–349, 2007. ISSN 09244247. doi: 10.1016/j.sna.2007.04.019.

[47] N. van Veen. Analytical Derivation of the Self-Alignment Motion of Flip Chip Soldered Components. *Journal of Electronic Packaging*, 121(2):116–121, jun 1999. ISSN 1043-7398. doi: 10.1115/1.2792665.

[48] G. M. Whitesides and B. Grzybowski. Self-assembly at all scales. *Science*, 295(5564):2418–2421, 2002. ISSN 00368075. doi: 10.1126/science.1070821.

[49] X. Xiong, Y. Hanein, J. Fang, Y. Wang, W. Wang, D.T. Schwartz, and K. F. Böhringer. Controlled multibatch self-assembly of microdevices. *Journal of Microelectromechanical Systems*, 12(2):117–127, 2003. ISSN 10577157. doi: 10.1109/JMEMS.2003.809964.

[50] Y. Zhang and J. I. D. Alexander. Sensitivity of liquid bridges subject to axial residual acceleration. *Physics of Fluids A*, 2(11):1966–1974, 1990. ISSN 08998213. doi: 10.1063/1.857672.

[51] W. Zheng, J. Chung, and H. O. Jacobs. Fluidic heterogeneous microsystems assembly and packaging. *Journal of Microelectromechanical Systems*, 15(4):864–870, 2006. ISSN 10577157. doi: 10.1109/JMEMS.2006.878885.

[52] Q. Zhou and B. Chang. Microhandling using robotic manipulation and capillary self-alignment. *IEEE International Conference on Intelligent Robots and Systems*, pages 5883–5888, 2006. doi: 10.1109/IROS.2006.282466.

A

Results Surface Evolver

This chapter shows some extra results that were found using the computational software Surface Evolver. This program finds surfaces that are shaped by surface tension and other surface energies [6]. From an initial stated surface, the surface evolves towards a minimum energy by a gradient descent method. Example results can be seen in Fig. A.1 and Fig. A.2.

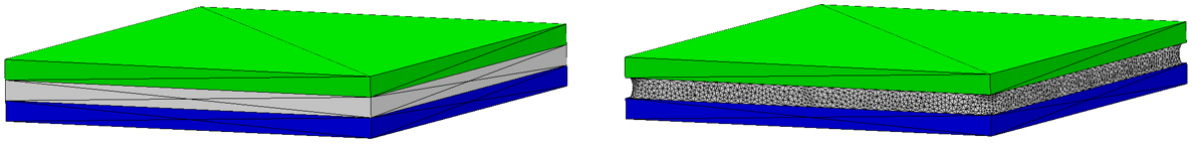

Figure A.1: Screenshots taken from Surface Evolver. System on the right is before evolving the surface, and on the right after evolving. Here, a chip of $1000 \times 1000 \times 50\mu m$ is used and lubricant height of $h_0 = 50\mu m$. Other parameters assumed to be in environmental conditions. Here, the green block represents the chip and the blue block the receptor.

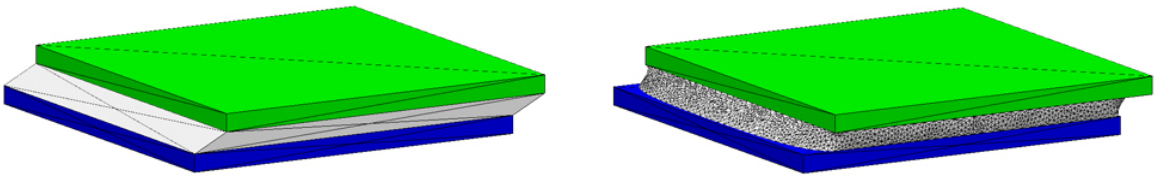

Figure A.2: Equivalent situation as described in Fig. A.1, only now a lateral shift of $x = 100\mu m$ of the top chip relative to the bottom receptor is introduced.

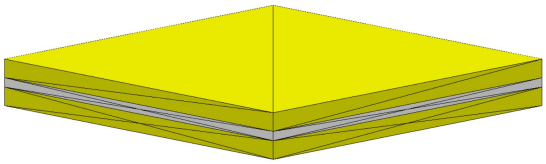

Figure A.3: Screenshot of Surface Evolver. Here, a $L = 1mm$ chip is connected to a receptor of equal dimensions with a liquid bridge with height $h_0 = 50\mu m$. This situation is before minimising the surface energy of the liquid.

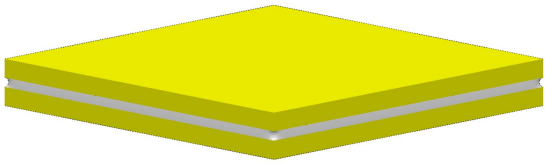

Figure A.4: Screenshot of the same system as described in the previous figure. After a fine convergence of the surface area.

Figure A.5: Front view of the system after a fine convergence.

Figure A.6: Diagonal cross-section of the system.

B

Linear State Space Model

The model described here was based on the case shown in section 2.3. Again, only a lateral displacement of the chip is considered and the meniscus is a deformable parallelepiped with a non-changing height h_0. Here, the capillary forces are surface tension and viscous forces. Since the surface tension is a force dependent on the absolute displacement between chip and receptor, it can translated into the lateral stiffness of the meniscus. The viscous force depends on the absolute velocity between chip and receptor and can therefore be seen as a damper. Now, the system can be approached as a mass connected with a damper and a spring to a massless cart [47]. Since the model is linear, it is expected to be less accurate than the previous described non-linear model. However, a state space model can still be very simple but powerful tool to find eigenfrequencies and oscillation characteristics.

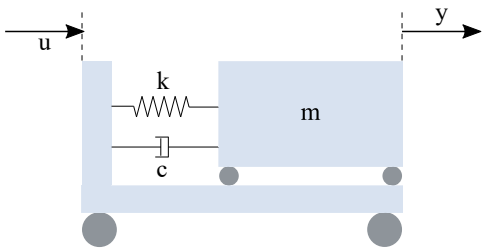

Figure B.1: Illustration showing a mass connected to a massless cart with a damper and a spring.

Here, the input u is the displacement of the receptor and the output y the position of the chip. The force balance of this situation is given as:

$$m\frac{\delta^2}{\delta t^2}y = c\left(\frac{\delta}{\delta t}u - \frac{\delta}{\delta t}y\right) + k(u-y) \tag{B.1}$$

where m equals the mass of the chip, and c and k represent the lateral damping and stiffness of the meniscus. This derivation can be rewritten and giving the transfer function of the system as

$$m\frac{\delta^2}{\delta t^2}y + \mathrm{c}\frac{\delta}{\delta \mathrm{t}}u + \mathrm{ky} = \mathrm{c}\frac{\delta}{\delta \mathrm{t}}u + \mathrm{ku} \tag{B.2}$$

$$H(s) = \frac{Y(s)}{U(s)} = \frac{cs+k}{ms^2+cs+k} \tag{B.3}$$

Since a state space system is per definition linear, a non-linear stiffness as given in 2.10 would not be applicable. However, the rightmost term of the restoring force 2.9 can be used to find the linear stiffness. Taking the derivative of this term with respect to the displacement x results in

$$k_l = \frac{\delta F_c}{\delta x} = \frac{2L\gamma}{h_0} \tag{B.4}$$

In case of a laminar flow between two plates a viscous force acts on both plates. Here, this force is proportional to the surfaces of the chip and receptor, difference in velocity of these and the height of the gap between them. The viscous force is then given by

$$F_v = \mu \frac{A\mathrm{v}}{h_0} = \mu \frac{L^2\mathrm{v}}{h_0} \tag{B.5}$$

where μ represents the dynamic viscosity and v the relative velocity between the receptor and chip. By taking the derivative of this force with respect to the relative velocity, the damping is found as

$$c = \mu \frac{L^2}{h_0} \tag{B.6}$$

C

Results Non-linear Model: Shift

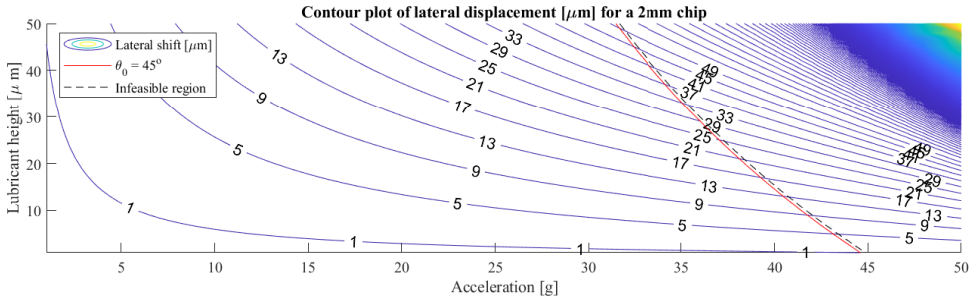

Figure C.1: Contour plot showing the lateral displacement of a 2mm chip on the contour lines. Lubricant height is varied along the y-axis and the acceleration along the x-axis. The red line shows where the infeasible region starts at which all combinations of the two variables result in an edge angle of $\theta = 45^o$. At higher values, the configuration will result in a failure.

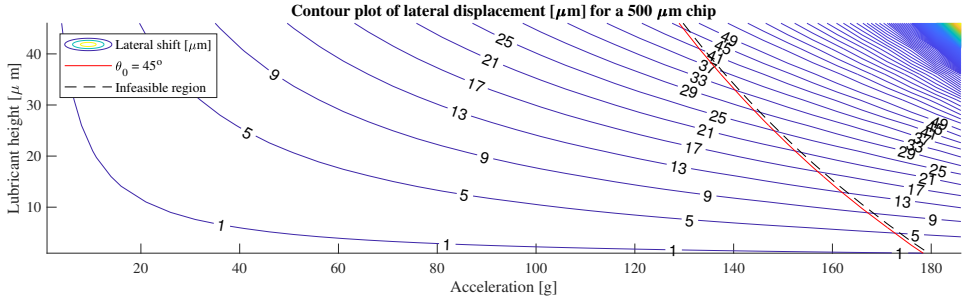

Figure C.2: Contour plot showing the lateral displacement of a 500μm chip.

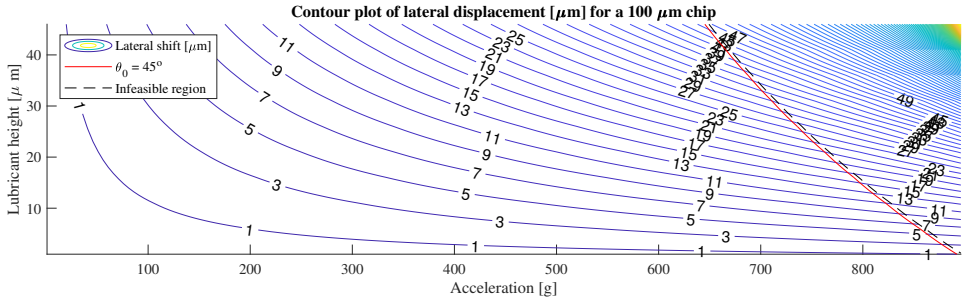

Figure C.3: Contour plot showing the lateral displacement of a 100μm chip.

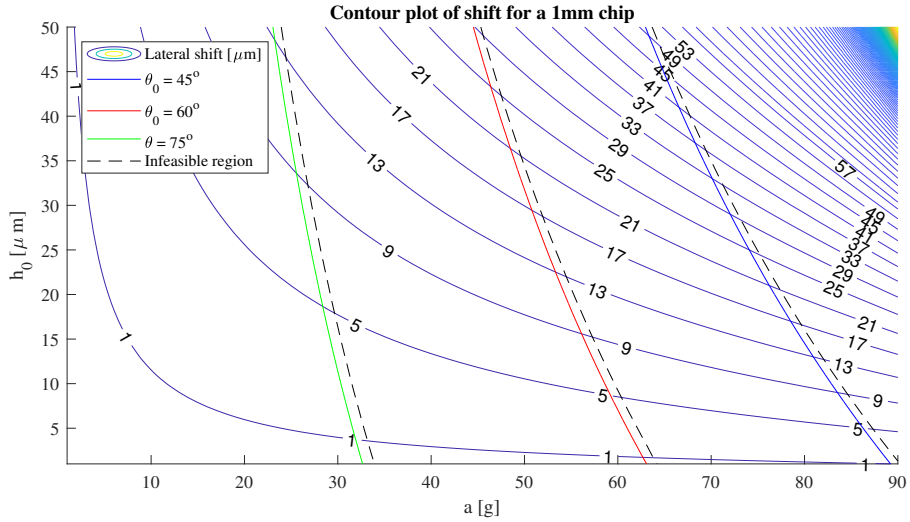

Figure C.4: Contour plot showing the lateral shift for different combinations of h_0 and a. The constraint lines indicate the maximum edge angles the system can reach before unpinning occurs. Here, contact angles are used of 45^o, 60^o and 75^o. The dashed lines indicate for every constraint where the infeasible region starts, e.g. where unpinning occurs.

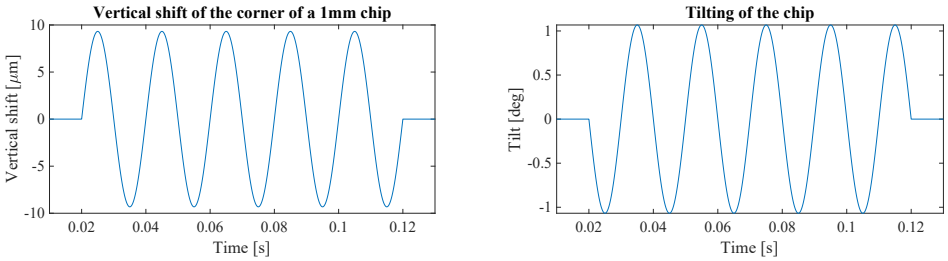

Figure C.5: Graph showing the vertical displacement of the top right corner of the top chip. Resulting from an acceleration of $a = 30g$ and a lubricant height of $h_0 = 30\mu m$.

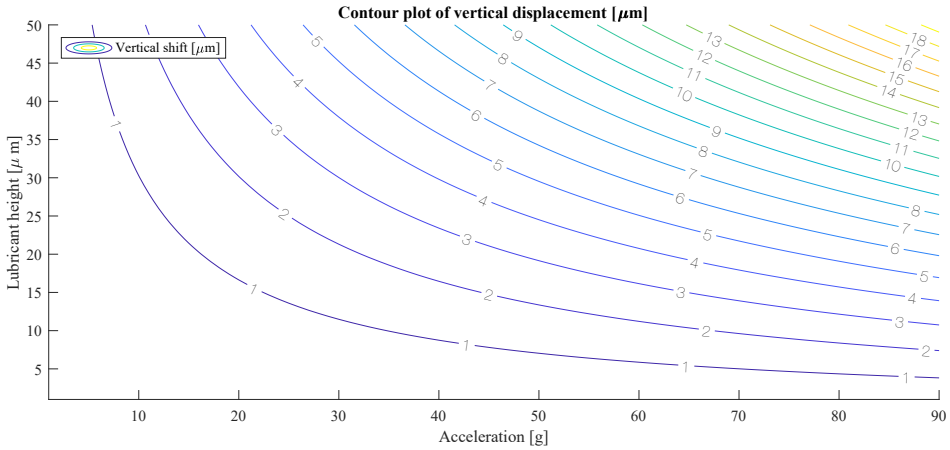

Figure C.6: Contour plot showing the vertical displacement of one of the corners of the top chip.

D

Geometrical Calculations

Edge Angles after Tilt Calculation

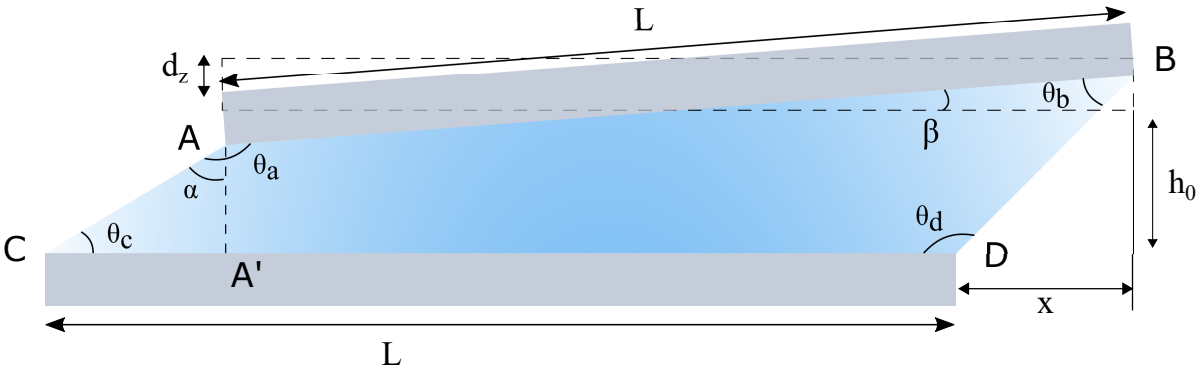

Figure D.1: Figure showing the necessary details to calculate all of the four edge angles.

In a tilted situation all of the four edge angles will have different values. A tilt is implemented by using the lateral shift that is calculated by the first model. The top chip is making a lateral shift relative to the receptor, and at exactly that position the left and right corners are lifted up- and downwards. The dashed lines indicate the position of the chip before tilt has taken place. The known values in this situation are therefore the chip dimensions and the lateral and vertical shift of the top left and right corners.

Calculating the four edge angles $\theta_a, \theta_b, \theta_c$) and θ_D is done as follows. First, the edge angle θ_c is found as

$$\theta_c = \text{atan}\left(\frac{h_0 - d_z}{x}\right) \tag{D.1}$$

The tilting angle the chip makes is found as

$$\beta = \text{asin}\left(\frac{2d_z}{L}\right) \tag{D.2}$$

And angle α with

$$\alpha = 180^o - 90^o - \theta_c \tag{D.3}$$

Next, the angle θ_a is found by summarising angles α, β and adding 90^o:

$$\theta_a = \alpha + \beta + 90^o \tag{D.4}$$
$$= 180^o + \beta - \theta_c \tag{D.5}$$
$$= 180^o + \text{asin}\left(\frac{2d_z}{L}\right) - \text{atan}\left(\frac{h_0 - d_z}{x}\right) \tag{D.6}$$

Then, angle θ_d is found as

$$\theta_d = 180^o - \text{atan}\left(\frac{h_0 + d_z}{x}\right) \tag{D.7}$$

Finally, the last angle θ_b can be found with the other three edge angles:

$$\theta_b = 360^o - \theta_a - \theta_c - \theta_d \tag{D.8}$$
$$= 90^o + 2\,\text{atan}\left(\frac{h_0 + d_z}{x}\right) + \text{atan}\left(\frac{h_0 - d_z}{x}\right) \tag{D.9}$$

Tilt Angle and Vertical Displacement Correction

Measuring the positions of all corners directly from the camera frame still contains a small error. In this case, the substrate is assumed to be moving in a perfect horizontal direction. However, in reality the substrate is always moving in a slightly tiled position. Therefore, the measured lateral and vertical displacement will always be slightly different. Compared to the lateral displacement, the error is much smaller and can therefore be neglected. However, for the vertical displacement this error is significant.

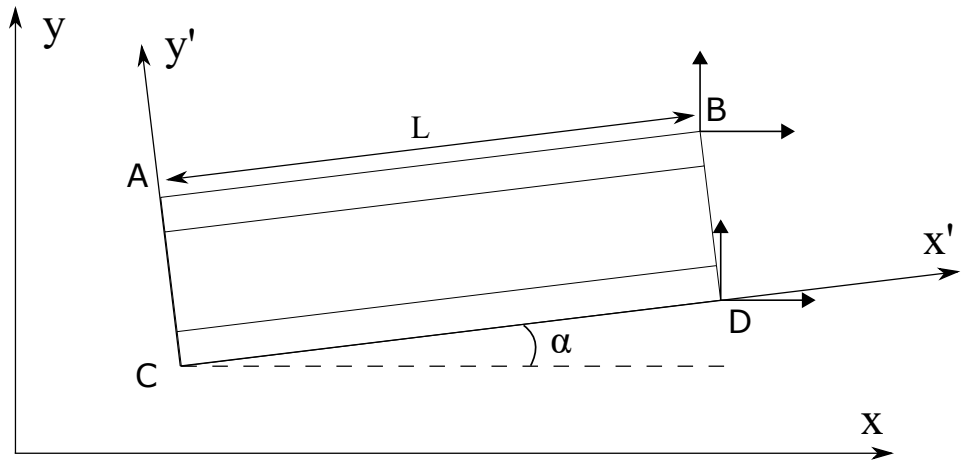

Figure D.2: Schematic representation of a front view of the system. The y- and x–axis refer to the reference frame of the camera. The y'- and x'-axis refers to the local reference frame of the chip.

If the vertical displacement is measured by taking the difference in y-position of the corners at A, B, C and D, an error due to the tilted angle of the substrate has not been taken into account. Here, the angle α represents the tilt angle of this substrate. The reference frame of the camera is indicated with y and x, whereas the local frame of the receptor is shown with a y'- and x'-axis. To find the net displacement between, for example, corners A and B, the difference should be taken in the local reference frame. These are given as:

$$v_l = \frac{A_y - C_y}{\cos(\alpha)} \tag{D.10}$$

$$v_r = \frac{B_y - D_y}{\cos(\alpha)} \tag{D.11}$$

Here, v_l and v_r represent the net vertical displacement on the left and right side of the chip. The corners indicated with a capital letter and subscript y, represent the y-coordinates measured in the reference frame of the camera.

E

Experimental Results

Start-Stop Phenomena

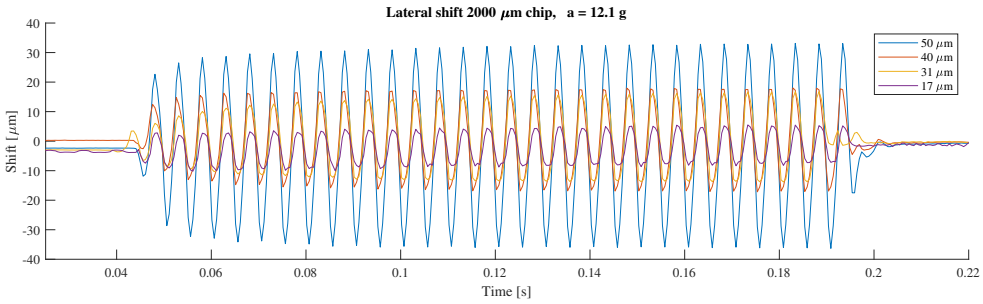

Figure E.1: Graph showing a variation in lubricant height h_0 and its effect to the relative lateral shift of the chip. Here, a 2mm sized chip has been used and accelerated at a maximum of 12.1g.

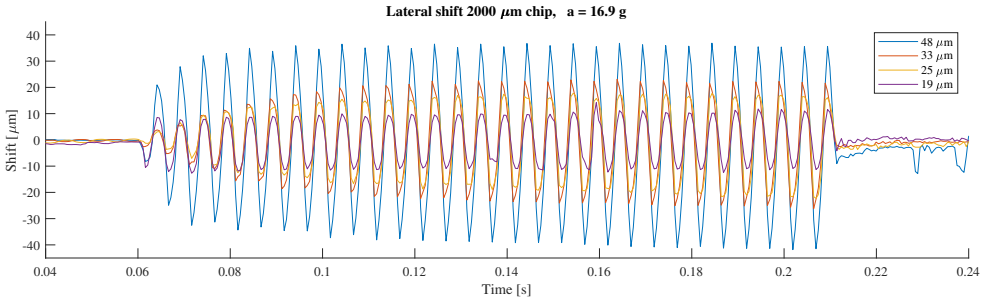

Figure E.2: Graph showing a variation in lubricant height h_0 and its effect to the relative lateral shift of the chip. Here, a 2mm sized chip has been used and accelerated at a maximum of 16.9g.

Effect of Different Accelerations

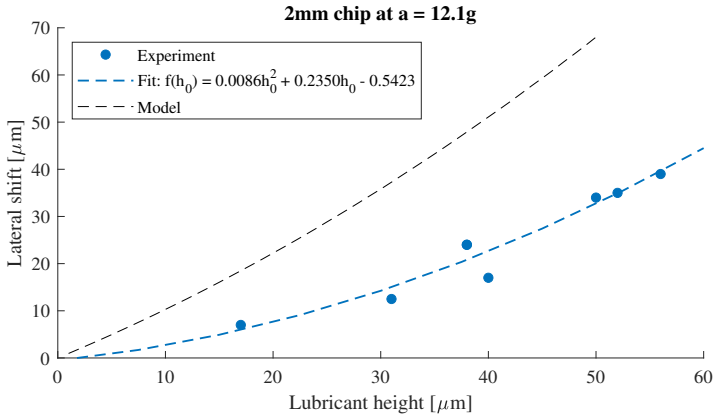

Figure E.3: Lateral shift of a 2mm chip at different lubricant heights. Coloured dashed line indicates a fitted polynomial of degree 2. Black dashed line represents the result from the model with equivalent parameters and variables.

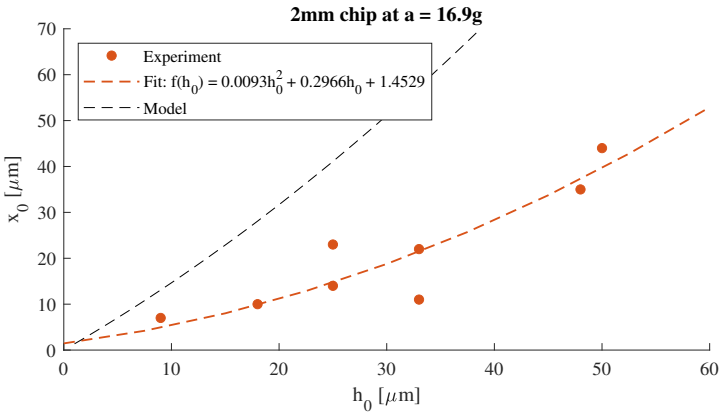

Figure E.4: Lateral shift of a 2mm chip at different lubricant heights. Coloured dashed line indicates a fitted polynomial of degree 2. Black dashed line represents the result from the model with equivalent parameters and variables.

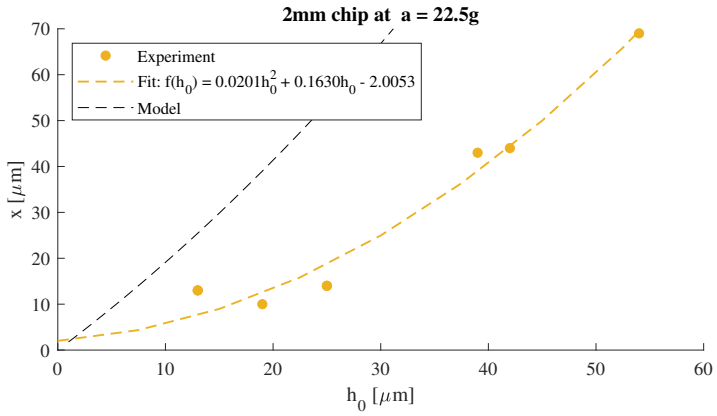

Figure E.5: Lateral shift of a 2mm chip at different lubricant heights. Coloured dashed line indicates a fitted polynomial of degree 2. Black dashed line represents the result from the model with equivalent parameters and variables.

Motion Comparison of Model and Experiment

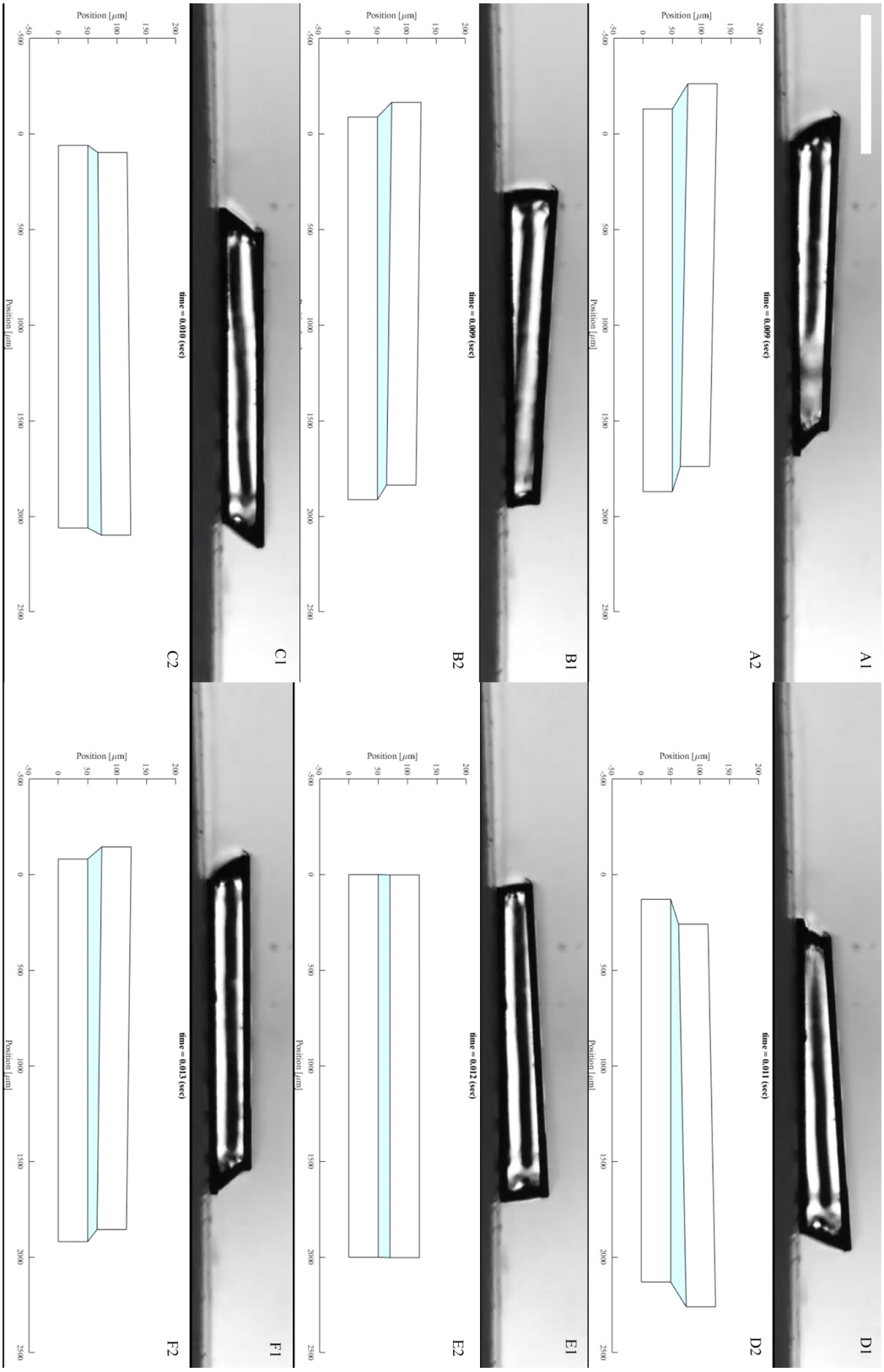

Figure E.6: Six screenshots of an experiment of a $L = 2mm$ chip oscillating at $f = 200Hz$ and $a = 7g$ compared to screenshots of the predicted motion of the model.

Results for Small Lubricant Height

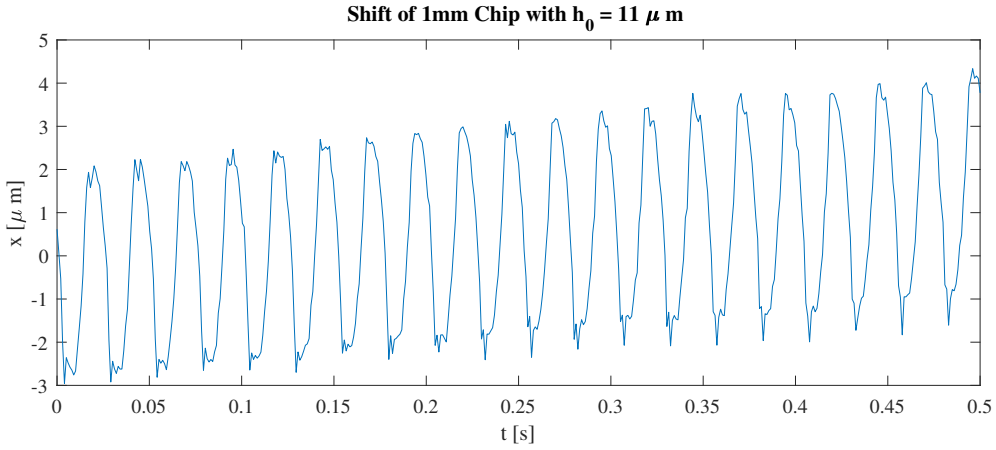

Figure E.7: Results of lateral shift for very small lubricant height $h_0 = 11\mu m$. A chip of $1mm$ was used and accelerated up to $a = 15g$.

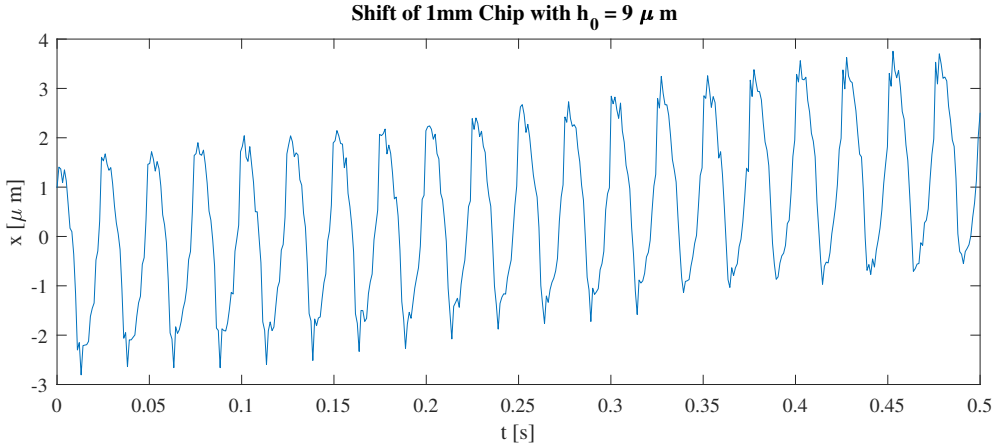

Figure E.8: Results of lateral shift for very small lubricant height $h_0 = 9\mu m$. A chip of $1mm$ was used and accelerated up to $a = 15g$.

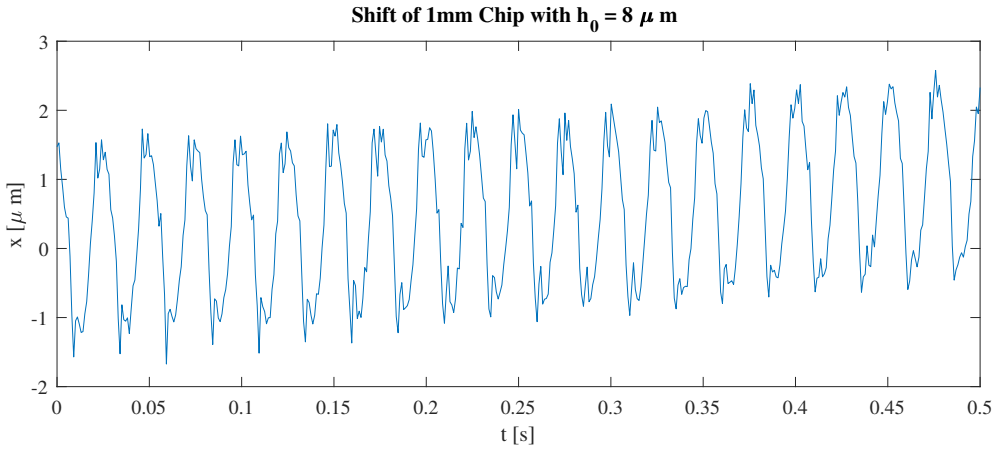

Figure E.9: Results of lateral shift for very small lubricant height $h_0 = 8\mu m$. A chip of $1mm$ was used and accelerated up to $a = 15g$.